

RESEARCH ARTICLE

10.1002/2016TC004294

This article is a companion to *Rutte et al.* [2017] doi:10.1002/2016TC004293.

Key Points:

- South and Central Pamir crust thickened from >37 to ~22 Ma and since ~12 Ma by thrust-sheet and fold-nappe emplacement
- Northward crustal collapse formed the Central Pamir gneiss domes at ~22–≥12 Ma by ~N-S extension during ongoing India-Asia convergence
- Pamir crustal evolution was governed by Indian slab breakoff and subsequent shallow underthrusting of cratonic Indian lithosphere

Supporting Information:

- Supporting Information S1
- Table S1
- Table S2
- Table S3
- Table S4
- Table S5
- Table S6
- Table S7
- Table S8
- Table S9
- Figure S1
- Figure S2

Correspondence to:

D. Rutte,
drutte@bgc.org

Citation:

Rutte, D., et al. (2017), Building the Pamir-Tibetan Plateau—Crustal stacking, extensional collapse, and lateral extrusion in the Central Pamir: 2. Timing and rates, *Tectonics*, 36, doi:10.1002/2016TC004294.

Received 29 JUN 2016

Accepted 7 JAN 2017

Accepted article online 11 JAN 2017

Building the Pamir-Tibetan Plateau—Crustal stacking, extensional collapse, and lateral extrusion in the Central Pamir: 2. Timing and rates

Daniel Rutte^{1,2} , Lothar Ratschbacher¹, Jahanzeb Khan^{1,3} , Konstanze Stübner^{1,4} , Bradley R. Hacker⁵ , Michael A. Stearns^{5,6}, Eva Enkelmann⁷ , Raymond Jonckheere¹, Jörg A. Pfänder¹, Blanka Sperner¹, and Marion Tichomirowa⁸

¹Geologie, TU Bergakademie Freiberg, Freiberg, Germany, ²Now at Berkeley Geochronology Center and Earth and Planetary Sciences, University of California, Berkeley, California, USA, ³Now at Geology, Azad Jammu and Kashmir University, Muzaffarabad, Pakistan, ⁴Now at Geowissenschaften, Universität Tübingen, Tübingen, Germany, ⁵Earth Sciences, University of California, Santa Barbara, California, USA, ⁶Now at Geology and Geophysics, University of Utah, Salt Lake City, Utah, USA, ⁷Geology, University of Cincinnati, Cincinnati, Ohio, USA, ⁸Mineralogie, TU Bergakademie Freiberg, Freiberg, Germany

Abstract Geothermochronologic data outline the temperature-deformation-time evolution of the Muskol and Shatput gneiss domes and their hanging walls in the Central Pamir. Prograde metamorphism started before ~35 Ma and peaked at ~23–20 Ma, reflecting top-to-~N thrust-sheet and fold-nappe emplacement that tripled the thickness of the upper ~7–10 km of the Asian crust. Multimethod thermochronology traces cooling through ~700–100°C between ~22 and 12 Ma due to exhumation along dome-bounding normal-sense shear zones. Synkinematic minerals date normal sense shear-zone deformation at ~22–17 Ma. Age-versus-elevation relationships and paleoisothersm spacing imply exhumation at ≥3 km/Myr. South of the domes, Mesozoic granitoids record slow cooling and/or constant temperature throughout the Paleogene and enhanced cooling (7–31°C/Myr) starting between ~23 and 12 Ma and continuing today. Integrating the Central Pamir data with those of the East (Chinese) Pamir Kongur Shan and Muztaghata domes, and with the South Pamir Shakh dara dome, implies (i) regionally distributed, Paleogene crustal thickening; (ii) Pamir-wide gravitational collapse of thickened crust starting at ~23–21 Ma during ongoing India-Asia convergence; and (iii) termination of doming and resumption of shortening following northward propagating underthrusting of the Indian cratonic lithosphere at ≥12 Ma. Westward lateral extrusion of Pamir Plateau crust into the Hindu Kush and the Tajik depression accompanied all stages. Deep-seated processes, e.g., slab breakoff, crustal foundering, and underthrusting of buoyant lithosphere, governed transitional phases in the Pamir, and likely the Tibet crust.

1. Introduction

At the northwestern tip of the India-Asia collision zone (Figure 1a), Cenozoic gneiss domes, bounded by normal-sense shear zones, cover ~30% of the Central, South, and East Pamir; together with their hanging walls, they expose the upper ~30–40 km of the crust (Figure 1b) [Schwab et al., 2004; Robinson et al., 2004; Schmidt et al., 2011; Stübner et al., 2013a]. The 60–70 km thick [Mechie et al., 2012] Pamir crust is underlain by a NW-convex arc of intermediate-depth seismicity interpreted to result from Asian lower crust and mantle that is delaminating and rolling back (the Asian slab; Figure 1c) [Schneider et al., 2013; Sippl et al., 2013a]. The Pamir gneiss domes allow insight into the processes and rates of the Cenozoic construction of the Asian crust in the Pamir-Tibetan Plateau and permit speculations about the interaction between deep crustal/upper mantle and middle-upper crustal processes.

In part 1 of this paper series, Rutte et al. [2017] detailed the geometry, kinematics, and amount of deformation during the evolution of the eastern Central Pamir—a history of convergence-driven, upper crustal thrust-sheet and midcrustal fold-nappe stacking, interrupted by synconvergent, orogen-normal, middle-upper crustal extension. The latter likely reflects dynamic adjustment of the Central Pamir to crustal thickening that was destabilized by deep lithospheric processes: Indian slab breakoff enhanced the gravitational potential energy stored in the thermally weakened crust of the Pamir Plateau and increased the basal heat flow; together with a weak foreland rheology, this resulted in extensional collapse of thick and high Plateau crust into the northern and western foreland depressions and in

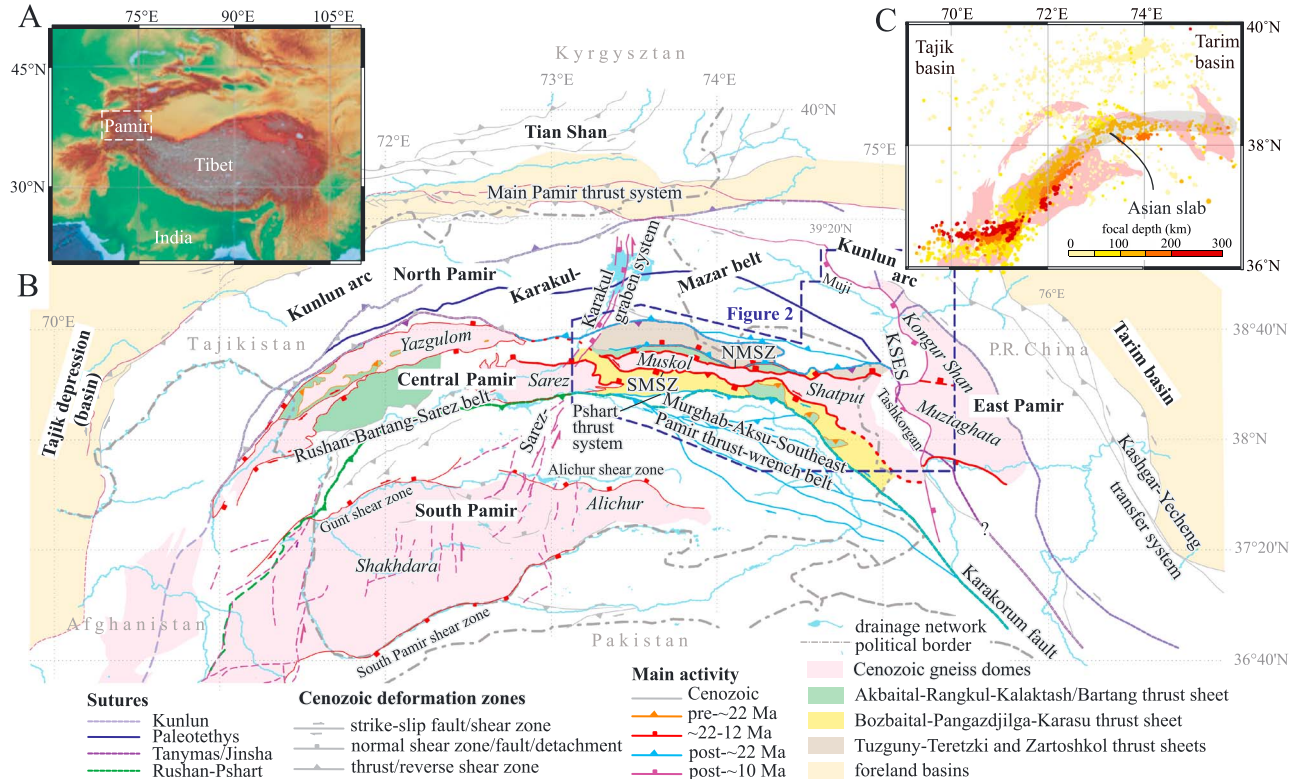


Figure 1. (a) Pamir orocline in the India-Asia orogenic system. (b) Tectonic overview of the Pamir orocline with Cenozoic gneiss domes, major Cenozoic faults, and Paleogene thrust sheets in the Central Pamir modified from Vlasov *et al.* [1991], Leven [1995], Schwab *et al.* [2004], Robinson *et al.* [2004, 2007], Stübner *et al.* [2013a], and Rutte *et al.* [2017]. NMSZ, North Muskol shear zone; SMSZ, South Muskol shear zone; KSES, Kongur Shan extensional system; Muji, Muji graben; Tashkorgan, Tashkorgan graben. (c) Intermediate-depth seismicity [Sippl *et al.*, 2013b] of the Asian slab plotted in relation to the Pamir gneiss domes.

core-complex formation on the Plateau [Stübner *et al.*, 2013a; Stearns *et al.*, 2013, 2015; Schurr *et al.*, 2014; Rutte *et al.*, 2017].

In the Paleogene, ~N-S shortening—coupled with orogen-parallel rock flow (lateral extrusion *sensu Ratschbacher et al.* [1991])—thickened the Central Pamir crust during prograde metamorphism. In the Miocene, ~N-S, normal-sense flow along the North (NMSZ) and South Muskol (SMSZ) shear zones exhumed the rocks of the Sarez, Muskol, and Shatput domes (Figure 1b) and imposed retrograde metamorphism. The change from contraction and peak metamorphism to exhumation and cooling occurred at ~23–20 Ma [Stearns *et al.*, 2013, 2015]. Since the late Miocene, ~N-S shortening and orogen-parallel extrusion have been re-imposed, forming out-of-sequence, bi-vergent thrust-fold belts along the dome margins and the Murghab-Aksu-Southeast Pamir thrust-wrench belt south of the domes (Figure 1b) [Rutte *et al.*, 2017]. Neotectonic conjugate strike-slip, normal faults within the Pamir (Kongur Shan extensional system and Sarez-Karakul graben system; Figure 1b) and thrusting along the Pamir’s northern front (Main Pamir thrust system; Figure 1b) imply a northward progression of deformation within a grossly similar kinematic framework dominated by ~N-S shortening and orogen-parallel extrusion [Schurr *et al.*, 2014; Sippl *et al.*, 2014]. Rutte *et al.* [2017] estimated >100 km (~70%) of N-S shortening and 17 to 75 km of N-S extension over the middle-upper crust of the eastern Pamir.

Herein, we address the following questions. When did the Central Pamir gneiss domes form? In particular, when did ~N-S extension begin and end, and at what rates did the gneiss-dome rocks exhume and cool? When were the predomant thrust sheets and fold nappes emplaced, and when were the postdoming thrust and wrench belts active? Ultimately, our radiometric dates constrain the times when the Asian crust reacted to deep-seated processes during the India-Asia collision. These processes include progressive thickening of Asian lithosphere following suturing of India with Asia at ~50 Ma [e.g., Klootwijk *et al.*, 1992; Najman *et al.*, 2010], Indian slab breakoff at ~25–20 Ma [e.g., Chung *et al.*, 2003; Replumaz *et al.*, 2010; DeCelles *et al.*, 2011;

Stearns et al., 2013], postbreakoff resumption of Indian underthrusting [e.g., *Kufner et al., 2016*], and formation of the seismic zone below the Pamir [*Sippl et al., 2013a*], when the cratonic mantle lithospheres of India (Cratonic India) and Asia (Cratonic Asia) collided at ~11 Ma [*Kufner et al., 2016*]. To address these questions, we employ multiple geothermochronometers, covering a temperature (T) range of ~700–100°C, dating rock samples from the eastern Sarez, Muskol, and Shatput domes and their hanging walls. We combine the dates with published ages on magmatism and metamorphism from the Central Pamir gneiss domes and the Muztaghata and Kongur Shan domes of the East (Chinese) Pamir [e.g., *Robinson et al., 2004, 2007, 2012; Schmidt et al., 2011; Thiede et al., 2013; Cao et al., 2013; Stearns et al., 2013, 2015*]. We find that N-S shortening and prograde metamorphism in the Central Pamir commenced prior to 35 Ma. N-S extensional exhumation began at ~23–20 Ma and presumably resulted from excess crustal thickening and was triggered by Indian slab breakoff. It ceased at ≥ 12 Ma due to decay of gravitational potential energy and underthrusting and northward propagation of cratonic Indian lithosphere. Lateral, westward collapse of the Pamir Plateau crust, manifested by orogen-parallel extension and dextral wrenching, occurred throughout the convergence history.

2. Tectonic Setting

The classic subdivision into the North, Central, and South Pamir reflects suturing of Gondwana-derived microcontinents and arcs to Asia during Paleozoic and early Mesozoic subduction-accretion [e.g., *Burtman and Molnar, 1993; Schwab et al., 2004*]. The East Pamir—mostly of North Pamir tectonostratigraphic affinity—comprises the Pamir east of the active Kongur Shan extensional system [e.g., *Robinson et al., 2012*]. Figure 1b illustrates the subdivision and locates the Cenozoic gneiss domes and major Cenozoic thrust sheets and fault zones. On a simplified geologic map of the eastern Central Pamir, Figure 2a presents the tectonostratigraphic units established by *Rutte et al. [2017]*, details the geographic names and geologic units, and locates the sites and samples discussed herein.

2.1. North Pamir: Main Pamir Thrust System and Pamir Foreland

Currently, the Pamir east of the Sarez-Karakul graben system (Figure 1b) moves north en bloc; at its northern boundary, it collides with the Tian Shan with high seismicity (Figure 1c) along the Main Pamir thrust system [*Schurr et al., 2014; Sippl et al., 2014*]. The western Pamir shows higher seismic deformation rates than the eastern Pamir, expressed by strike-slip and normal-faulting events, indicating ~E-W extension together with ~N-S shortening. *Schurr et al. [2014]* explained the active deformation by (i) dominant ~northward motion of the Pamir over the Tajik and Tarim cratonic basins, with the bulk of the deformation absorbed along the Main Pamir thrust system, and (ii) westward gravitational collapse of the Pamir Plateau into the Tajik depression, where thin-skinned shortening inverts the Tajik basin above an evaporitic décollement. The superposition of Pamir's bulk northward movement and westward (lateral) extrusion causes the gradual rotation of surface velocities from ~NNW to ~WNW observed by GPS measurements [*Zubovich et al., 2010; Ischuk et al., 2013*]. Deformation along the Main Pamir thrust system initiated at ~25–16 Ma [e.g., *Sobel and Dumitru, 1997; Coutand et al., 2002*] but intensified later (e.g., ~15–10 Ma onset of inversion of the Tajik basin and reactivation of the southwestern Tian Shan [*Käbner et al., 2016*]; ~10–6 Ma, Kashgar–Yecheng transfer system [*Cao et al., 2013*]; >12 – ≤ 6 Ma, Kuke fault of the Chinese Pamir [*Sobel et al., 2011*]; and ~6–5 Ma, Takegai and Kenenbieerte thrusts, Chinese Pamir [*Thompson et al., 2015*]). Similarly, first conglomeratic deposits shed from the Pamir appear in the Upper Oligocene-Lower Miocene strata of the northwestern Tajik basin. Massive deposition with significant erosion of the North Pamir and basin inversion commenced in the Middle-Late Miocene, highlighted by growth strata (~11 Ma) and angular unconformities [*Forsten and Sharapov, 2000; Klocke et al., 2015*]. The North Pamir—south of the Main Pamir thrust system and north of the Central Pamir gneiss domes—shows <10 km exhumation since the Late Triassic; *Amidon and Hynek [2010]* correlated two periods of accelerated exhumation at ~50–40 Ma and ~25–16 Ma with far-field effects of the early India-Asia collision and breakoff of the Indian slab or slip on the nascent Karakorum fault, respectively.

2.2. Eastern Central and Southeast Pamir: Muskol-Shatput Gneiss Domes and Their Hanging Walls

Pre-Cenozoic structures are little studied and difficult to trace due to Cenozoic reactivation and overprint [*Rutte et al., 2017*]. Exceptions include the Cimmerian angular unconformity at the base of the Jurassic, and related pre-Jurassic, N-NE trending, tight folds and thrusts in the southeast Pamir [e.g., *Dronov et al., 2006*;

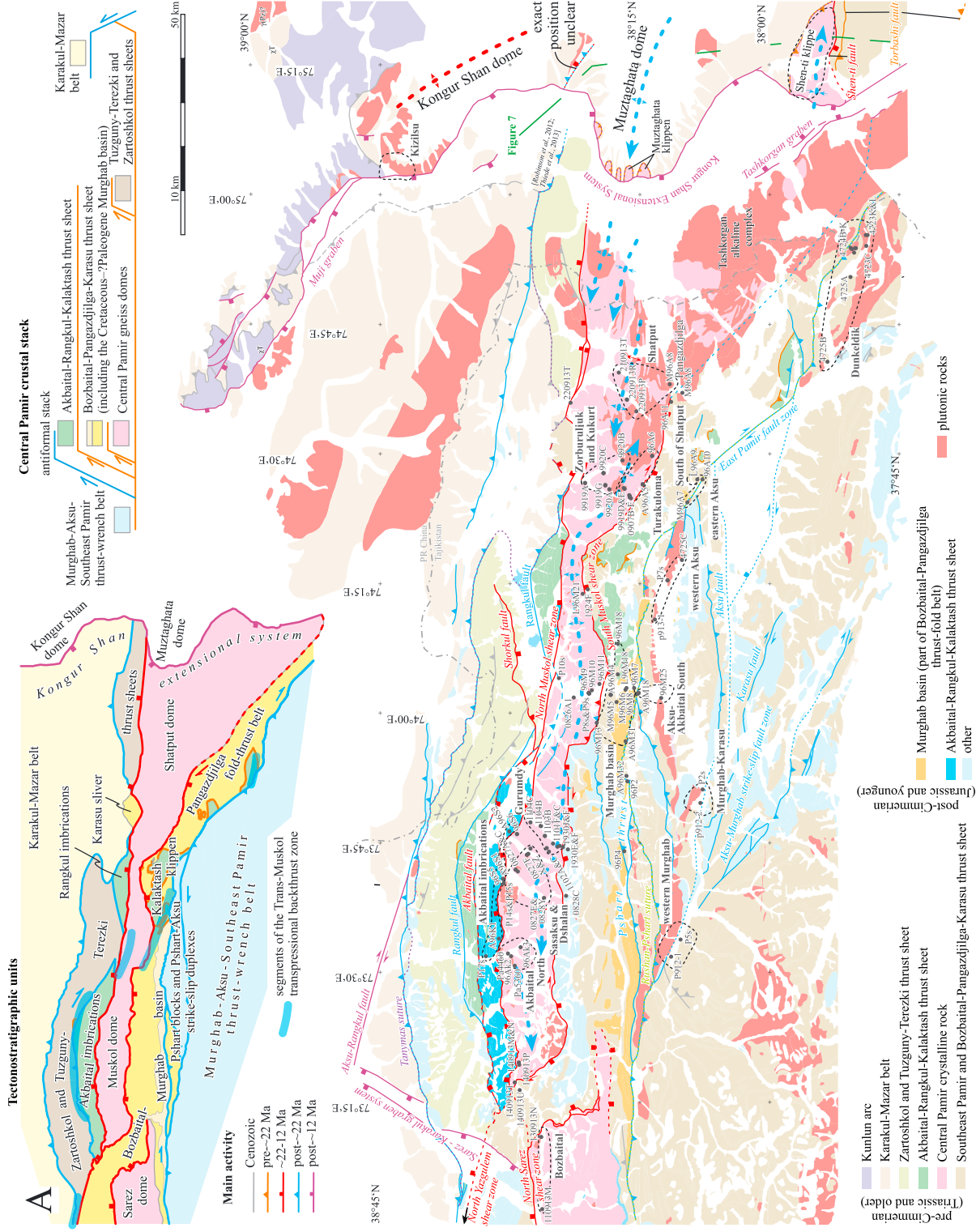


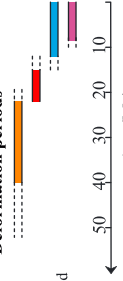
Figure 2. (a) Simplified geologic-structural map of the eastern Central Pamir with the Cenozoic tectonostratigraphic units, relative thrust sequence, major faults (coloring refers to the main activity of the deformation phases established in *Rutte et al.* [2017]), pre-Cimmerian and post-Cimmerian stratigraphy, geographic names, and sites and samples discussed in this work. The insets at top show the major tectonic units, their main activity, and their relative position in the thrust-fold nappe stack of the Central Pamir. (b) High-temperature geothermochronometric ages from this work and *Schmalholz* [2004], *Robinson et al.* [2004, 2007], and *Stearns et al.* [2013, 2015]; symbols and colors indicate method and date, respectively. (c) The $^{40}\text{Ar}/^{39}\text{Ar}$ mica dates from this work and *Arnaud et al.* [1993], *Robinson et al.* [2004, 2007, 2010], *Sobel et al.* [2011, 2013], *Stübner et al.* [2013b], and *Thiede et al.* [2013]. Rectangles indicate swaths along which the thermochronologic data were projected; the overlapping dates imply a cooling age interpretation. (d) Probability density distributions of $^{40}\text{Ar}/^{39}\text{Ar}$ mica ages from the Muskol and Shatput domes differentiating between two phases of Cenozoic deformation; the temperature thermochronometric data from this work, *Arnaud et al.* [1993], *Stübner et al.* [2011, 2013], *Thiede et al.* [2013b], *Thiede et al.* [2013], and *Cao et al.* [2013]. (f) Low-

F Low-temperature thermochronology

- < 4 Ma ▲ (U-Th-Sm)/He apatite (AHe)
- 4 - 8.5 Ma ● (U-Th)/He zircon (ZHe)
- 8.5 - 19 Ma ◆ Apatite fission track (AFT)
- 19 - 26 Ma ◆ K-Ar sericite
- > 26 Ma ★ Apatite fission track length measured (see appendix Figure S2)

- thrust
- normal fault
- strike-slip fault
- major fold

Deformation periods



area represented by one time-temperature diagram in Figure 4

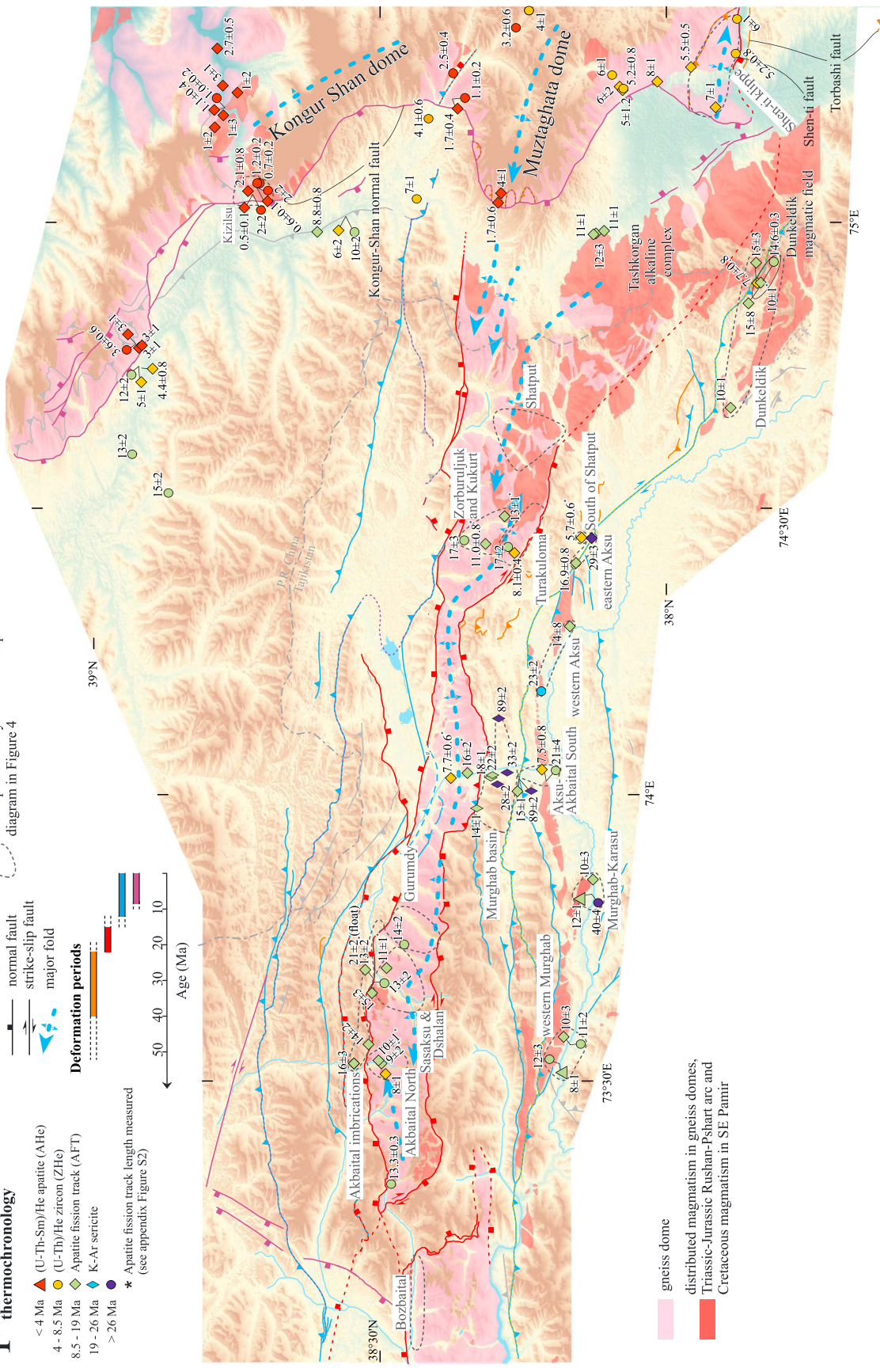


Figure 2. (continued)

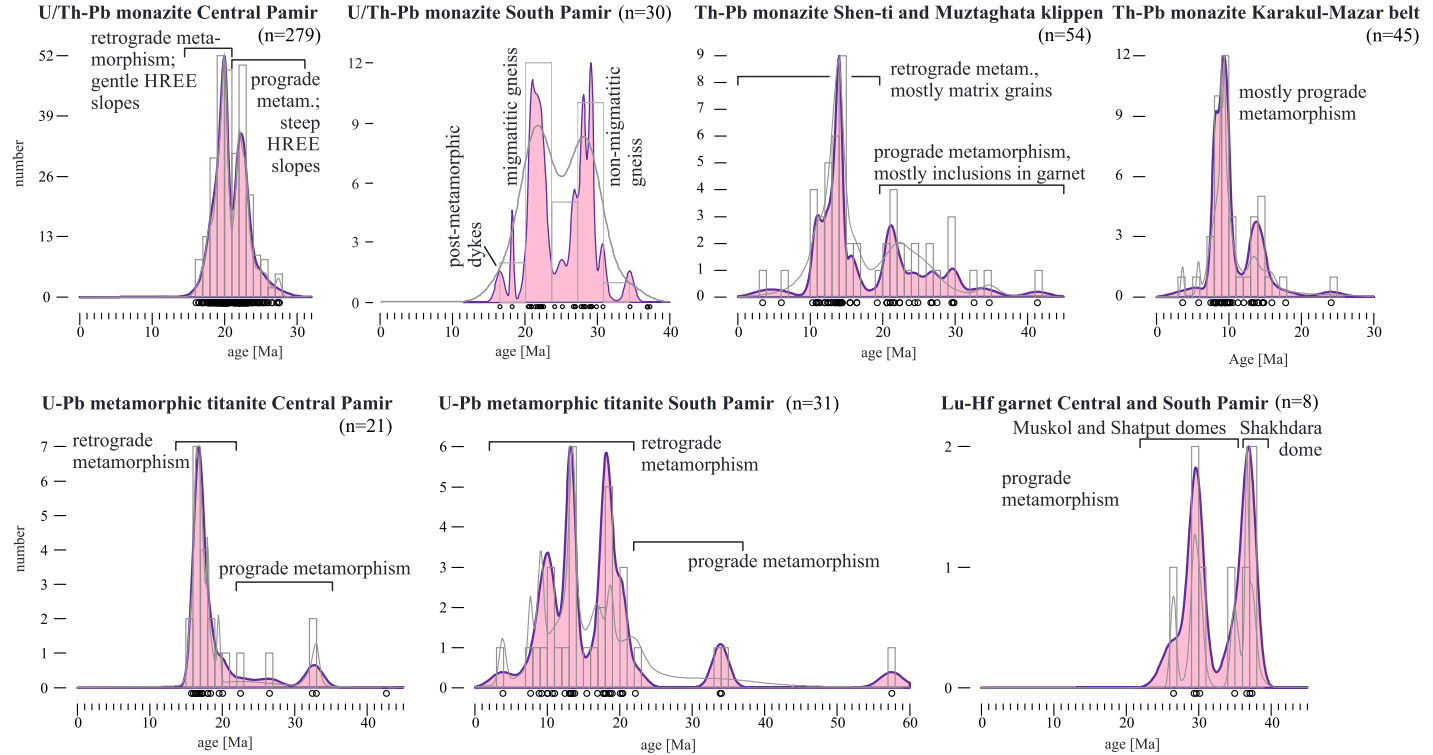


Figure 3. Published high-temperature geothermochronologic data from the South, Central, and East Pamir, displayed in histograms, probability density functions (grey line), and kernel-density estimate curves (filled area; see Vermeesch [2012] for definition and implementation). Ages from Robinson *et al.* [2004, 2007], Stearns *et al.* [2013, 2015], and Smit *et al.* [2014].

Angiolini *et al.*, 2014]. The Cenozoic Central Pamir contains four major upper crustal allochthons that form a Paleogene, top-to- \sim N, \sim 30–40 km thick crustal stack (Figure 2a) [Rutte *et al.*, 2017]. Its sole thrust reactivated the south dipping, Triassic Tanyamas suture zone, which contains Carboniferous-Permian Karakul-Mazar belt accretionary-wedge rocks of the North Pamir in its footwall (Figure 1b) [Schwab *et al.*, 2004]. The Tuzguny-Terezki and Zartoshkol thrust sheets constitute the leading edge. The other units form an antiformal stack (Figure 2a). The deepest allochthons crop out in the gneiss domes, which are asymmetric, partly overlapping antiforms with approximately east trending axes that extend \sim 10–40 km N-S and $>$ 400 km E-W from the Afghan to the Chinese Pamir (Figure 1b). Lu-Hf garnet (Grt; \sim 35–26 Ma) [Smit *et al.*, 2014], U/Th-Pb monazite (Mnz; \sim 28–14 Ma) [Robinson *et al.*, 2007; Stearns *et al.*, 2013], and U-Pb titanite (Ttn; \sim 36–19 Ma) [Stearns *et al.*, 2015] ages—compiled in Figure 3—date the prograde, crustal-thickening history of these crystalline rocks. The gneisses comprise a $>$ 4.5 km thick succession of Ediacaran to Permian—possibly Triassic—volcanoclastic rocks, folded in meter to kilometer-scale tight to isoclinal, recumbent folds bounded by thrusts, forming fold nappes. The dome rocks were overthrust by the Bozbaital-Pangazdjilga-Karasu thrust sheet consisting of Carboniferous to Cretaceous, likely Paleogene strata, metamorphosed to chlorite (Chl), and biotite (Bt) grade, which in turn was overthrust by the Akbaital-Rangkul-Kalaktash thrust sheet consisting of Cambrian to Cretaceous strata; it shows Chl, locally Bt-grade metamorphism. These four allochthons imbricated an \sim 7–10 km thick succession, stretching $>$ 150 km N-S prior to deformation. About E-W, orogen-parallel stretching and dextral wrenching occurred coevally with crustal stacking. Rutte *et al.* [2017] related the Paleogene, orogen-parallel \sim E-W stretching to westward lateral extrusion of Central Pamir rocks into the Afghan Hindu Kush, an area west of the frontal India-Asia collision.

Starting at \sim 23–20 Ma [Stearns *et al.*, 2013, 2015; this study], normal-sense shear zones dissected part of the crustal stack and exhumed its deepest part as the Central Pamir gneiss domes. Today, the Bozbaital-Pangazdjilga fold-thrust belt, as a part of the Bozbaital-Pangazdjilga-Karasu thrust sheet, forms most of the southern hanging wall of the Muskol-Shatput domes above the SMSZ; the Akbaital-Rangkul imbrications, as a part of the Akbaital-Rangkul-Kalaktash thrust sheet, constitute most of the northern hanging wall of the Muskol-Shatput domes above the NMSZ (Figure 2a). North of the domes, faults, both synthetic and

antithetic to the NMSZ, accommodated distributed extension. *Rutte et al.* [2017] attributed extension to reflect ~N-S gravitational adjustment of thickened crust that was destabilized by Indian slab breakoff. Following crustal extension, continued ~N-S shortening inverted the normal-sense shear zones, reactivated older fold-thrust structures, and formed the dextral-transpressive Trans-Muskol transpressional back thrust zone (Figure 2a). Farther south, the Aksu-Murghab-Southeast Pamir thrust-wrench belt (Figure 2a) shows ~N-S shortening interacting with ~E-W extension along mostly dextral faults and shear zones. The Pshart thrust system, the leading fault of this thrust-wrench belt, is a major out-of-sequence thrust, reactivating the Jurassic Rushan-Pshart suture between the Central and South Pamir. *Rutte et al.* [2017] related ~E-W extension and dextral wrenching to lateral extrusion of the South and Central Pamir crust and its collapse into the Tajik depression.

At ~11 Ma the Tashkorgan alkaline igneous complex including the Dunkeldik pipe field was emplaced in the eastern Shatput dome and its southern hanging wall [*Ducea et al.*, 2003; *Jiang et al.*, 2012]. Crustal xenoliths from the Dunkeldik volcanic rocks were metamorphosed at 60–100 km depth prior to eruption [*Hacker et al.*, 2005; *Gordon et al.*, 2012]; detrital zircons constrain their protoliths to be of South Pamir origin [*Ducea et al.*, 2003]. *Hacker et al.* [2005] and *Gordon et al.* [2012] suggested two possible mechanisms for the burial of this material: transient crustal dripping or subduction erosion by underthrusting Indian lithosphere. *Jiang et al.* [2012] inferred the melts of the potassic granitic-syenitic intrusions to be sourced from asthenospheric material at 70–100 km depth and suggested asthenospheric upwelling as a trigger for melting.

2.3. Southwest Pamir: Shakh dara-Alichur Domes

The Shakh dara-Alichur domes expose the largest tract of Cenozoic middle-upper crustal rocks in the Pamir (Figure 1b) [*Stübner et al.*, 2013a]. The Proterozoic-Mesozoic volcano-sedimentary and Cretaceous magmatic arc rocks exposed in the Shakh dara dome experienced shortening prior to and synchronous with upper amphibolite to granulite-facies metamorphism (0.6–1.5 GPa, 600–800°C) [*Schmidt et al.*, 2011; *Stearns et al.*, 2015] that culminated in regional migmatization. The Shakh dara dome gneisses were exhumed top-to-~SSE along the ~30° dipping South Pamir shear zone that bounds the dome in the south. The mostly low-grade Gunt shear zone (Figure 1b) forms the northern dome boundary; there, early top-to-~N transtensional shear fabrics were folded into a subvertical zone and overprinted by dextral shear. The Alichur shear zone (Figure 1b) bounds the smaller Alichur dome in the north and exhumed rocks from ~10–20 km depth. *Stearns et al.* [2013, 2015] and *Smit et al.* [2014] dated prograde, thickening-related metamorphism in the Shakh dara dome between ~37 and 22 Ma, and *Stübner et al.* [2013a] and *Stearns et al.* [2015] dated exhumation along the normal-sense shear zones at ~21–2 Ma with cooling rates of 30–90°C/Myr. Cooling began at ~21–20 Ma along the Gunt shear zone and progressed southward from ~18–15 to ~4–2 Ma along the dome-spanning South Pamir shear zone. Thereafter, ~N-S extension was replaced by ~N-S shortening and ~E-W extension along strike-slip and normal faults [*Schurr et al.*, 2014].

2.4. East Pamir: Kashgar-Yecheng Transfer Fault System and Kongur Shan Extensional System

The dextral Kashgar-Yecheng transfer system in the Chinese Pamir accommodated ~280 km dextral displacement of the Pamir relative to the Tarim craton (Figure 1b) [*Cowgill*, 2010]. Whether this offset is transferred to the Main Pamir thrust system is unclear, as younger rocks cover possible connecting faults. Subsurface data imply the presence of a right-stepping fault geometry active in the early Miocene, with the development of a pull-apart within the western Tarim basin, and a (partial?) northward slip transfer east of the Pamir, possibly to the Talas-Ferghana fault system [*Wei et al.*, 2013; *Bande et al.*, 2015]. Using partially reset detrital apatite fission track (AFT) ages from foreland-basin strata, *Sobel and Dumitru* [1997] suggested that deformation along the Kashgar-Yecheng transfer system commenced at ~25–18 Ma; *Bershaw et al.* [2012], using detrital U-Pb zircon data, and *Cao et al.* [2013], using AFT data, argued for ~10–6 Ma. Motion along the transfer system stopped at ~5–3 Ma, when Tarim and the Pamir started to move synchronously [*Sobel et al.*, 2011].

The dextral Karakorum fault zone likely connects with the Murghab-Aksu-Southeast Pamir thrust-wrench belt in the southeast Pamir (Figure 1b) [*Strecker et al.*, 1995]. The Karakorum fault offsets Triassic-Jurassic carbonates by ~150–165 km in the southeast Pamir and Karakorum [*Robinson*, 2009a]. *Robinson* [2009b] documented several generations of up to ~200 ka old strata covering the northern Karakorum fault, indicating no younger deformation. *Schurr et al.* [2014] reported 15–20 km deep earthquakes—two with dextral fault plane

solutions on NW-striking planes—tracing the Aksu-Murghab strike-slip zone (Figure 2a) southeast toward the Karakorum fault.

The N to NW striking Kongur Shan extensional system has the Muji and Tashkorgan grabens in its hanging wall [Robinson *et al.*, 2004, 2007]; the latter bounds the Shatput dome to the east (Figure 2a). The active top-to- \sim W Kongur Shan normal fault (Figure 2b) is responsible for most of the exhumation of the Kongur Shan and some of the exhumation of the Muztaghata-dome rocks. The Kongur Shan dome trends NNW and exposes amphibolite-facies metamorphic rocks of North Pamir (Karakul-Mazar belt and Kunlun arc) affinity (U-Pb detrital zircon ages [Robinson *et al.*, 2012]). Monazite hosted in prograde-zoned Grt at the northern tip of the Kongur Shan dome yielded Th-Pb ages of \sim 10.2–9.0 (mean \sim 9.3) Ma interpreted as crustal thickening within the Main Pamir thrust system; \sim 9.0–3.6 Ma matrix Mnz dates were interpreted to reflect peak or retrograde recrystallization [Robinson *et al.*, 2004]. $^{40}\text{Ar}/^{39}\text{Ar}$ white mica and Bt (ArWm and ArBt, respectively), zircon (U-Th)/He (ZHe), and AFT cooling ages range from \sim 4.8 to 0.5 Ma (Figures 2b to 2f) [Arnaud *et al.*, 1993; Robinson *et al.*, 2004, 2010; Thiede *et al.*, 2013; Cao *et al.*, 2013]. $^{40}\text{Ar}/^{39}\text{Ar}$ K-feldspar (ArKfs) spectra indicate significant amounts of excess ^{40}Ar ; those least affected may indicate cooling from \sim 8 Ma onward [Arnaud *et al.*, 1993; Robinson *et al.*, 2004]. Robinson *et al.* [2004] proposed \sim 8–7 Ma as the minimum age of initiation of extension along the Kongur Shan normal fault, based on multi-diffusion domain analysis of one K-feldspar (Kfs) sample, and on two-dimensional thermal-kinematic models using ArWm and ArBt data.

The Muztaghata gneiss dome trends \sim WNW and is a \sim S vergent antiform. Robinson *et al.* [2007] correlated it with the Shatput dome, with the Shen-ti fault as the equivalent of the SMSZ (Figure 2a). Most of the dome has North Pamir (Karakul-Mazar belt) protoliths (U-Pb detrital zircon ages), whereas its upper section (Muztaghata and Shen-ti klippen; Figure 2a) yielded detrital U-Pb zircon ages and ϵ_{Nd} values of Central Pamir affinity, with the Tanymas suture between the Central and the North Pamir being exposed at the western flank of the Muztaghata dome [Robinson *et al.*, 2012]. The amphibolite-facies migmatitic schists of the Shen-ti klippe host coexisting kyanite (Ky) and Kfs, indicating that migmatization (muscovite-dehydration melting) began close to the peak-metamorphic conditions at \sim 700°C, \geq 0.8 GPa. To date metamorphism in the rocks of these klippen, Robinson *et al.* [2007] analyzed Mnz and obtained Th-Pb dates ranging from \sim 175 to \sim 7.5 Ma (Figures 2b and 3). Cenozoic Mnz included in Grt yielded 30 ± 5 to 19 ± 1 Ma ($n=13$) and 16 ± 3 to 11 ± 1 Ma ($n=6$; all uncertainties in this paper are reported at the 2σ level); the latter was termed the \sim 14 Ma group. Matrix ages are mostly <20 Ma. Robinson *et al.* [2007] interpreted these ages to indicate Oligocene-Early Miocene prograde metamorphism, \sim 14 Ma migmatization, and subsequent exhumation/cooling with Mnz recrystallization. ArWm, ArBt, ZHe, zircon fission track (ZFT), and AFT cooling ages range from 13.7 ± 0.4 to 1.1 ± 0.1 Ma (Figures 2c to 2f) [Robinson *et al.*, 2007; Sobel *et al.*, 2011; Cao *et al.*, 2013; Thiede *et al.*, 2013]. Cao *et al.* [2013] determined cooling rates of \sim 125 and \sim 190°C/Myr for the Muztaghata and Kongur Shan domes, respectively.

3. Methods

Table S1 in the supporting information provides geographically grouped sample locations (Figure 2a), lithologic descriptions, and data on key geochronologic samples from previous work. Tables S2 to S8 list our radiometric data. Below, we specify our methodology and closure-temperature (T_c) estimates.

3.1. Sample Processing

We fragmented samples either by high-voltage discharge employing the Freiberg SELFRAG® facility or by jaw crusher. Mineral concentrates were enriched by magnetic separation, wet and dry shaking tables, heavy liquids, and by handpicking.

3.2. $^{40}\text{Ar}/^{39}\text{Ar}$ and K-Ar Analysis

For $^{40}\text{Ar}/^{39}\text{Ar}$ analysis, we used the largest grain-size fraction from which we could handpick optically inclusion-free crystals. The SELFRAG® processing yields grain sizes corresponding closely to the true crystal size; additionally, it minimizes the proportion of broken grains [Sperner *et al.*, 2014]. We carried out $^{40}\text{Ar}/^{39}\text{Ar}$ analysis at three laboratories: Stanford University, the Argon laboratory of the Slovak Academy of Sciences (SEAL), and the Argonlab Freiberg (ALF) laboratory at the Technische Universität (TU) Bergakademie Freiberg. Hacker *et al.* [1996] and Frimmel and Frank [1998] described the analytical procedures and age standards used in the Stanford and SEAL laboratories, respectively. Pfänder *et al.* [2014] detailed the

analytical procedures for the ALF laboratory, and *Rutte et al.* [2015] detailed the irradiation geometry and reactor specifics used for the ALF samples, which comprise the majority of the reported ages; additional to age standards, metallic fluence monitors were used to correct for horizontal fluence gradients in some irradiations (Table S2). We used the revised age-standard values of *Renne et al.* [2010, 2011] for the calculation of the ages from all laboratories (ALF and SEAL: Fish-Canyon sanidine at 28.305 ± 0.072 Ma; Stanford: Taylor-Creek sanidine at 28.608 ± 0.066 Ma). We calculated weighted mean (WMA) and (inverse) isochron ages (IIA/IA) and their statistical uncertainties (Table S2) with Isoplot [Ludwig, 2008]. Most samples yielded well-defined plateau ages for which we report the WMA. For samples exhibiting argon loss, we used a WMA comprising the steps defining a plateau with atmospheric $^{40}\text{Ar}/^{36}\text{Ar}$ isochron intercepts. For samples with a trapped Ar component of nonatmospheric composition, i.e., containing extraneous argon (terminology of *Dalrymple and Lanphere* [1969] and *McDougall and Harrison* [1999]), we used the least disturbed steps with atmospheric intercepts or the IIA, in the case of evenly distributed trapped nonatmospheric argon. In the latter case, we also recalculated the WMA using the nonatmospheric $^{40}\text{Ar}/^{36}\text{Ar}$ intercept. For a few samples with a variable age spectrum and a weakly disturbed isochron, we report an age that covers the combined uncertainties of the WMA and IIA. Figure S1 in the supporting information shows age-spectrum plots of all analyzed samples and selected isochron plots.

We analyzed metabasalt and sericite with the K-Ar technique at the Russian Academy of Sciences, St. Petersburg (Table S3). All whole-rock basalt samples were crushed to fine powder to destroy bubbles that might contain extraneous ^{40}Ar . We obtained $<2 \mu\text{m}$ sericite fractions by the Atterberg technique. The content of radiogenic ^{40}Ar was measured by isotope dilution with ^{38}Ar as the isotope tracer, and the K concentration was determined in duplicate by flame photometry.

3.3. Apatite Fission Track Analysis

The AFT data (Table S4) were determined with the external detector method [e.g., *Gleadow*, 1981] and the ζ approach [e.g., *Hurford and Green*, 1983]. The apatite mounts were etched for 20 s in 5.5 M HNO_3 at 21°C [*Carlson et al.*, 1999]; covered with 1 cm^2 of $50 \mu\text{m}$ thick, U-free muscovite external detectors; stacked in irradiation containers with three to four age-standard mounts (Durango apatite: 31.4 ± 0.1 Ma [*McDowell et al.*, 2005] and Fish-Canyon tuff apatite: 28.2 ± 0.1 Ma [*Gleadow et al.*, 2015]) and standard uranium glasses (IRMM-450R); and irradiated in the hydraulic channel of the FRM-II reactor at the TU Munich, Germany. We etched the external detectors for 30 min in 48% HF at room temperature and repositioned them track-side down on the apatite mounts [*Jonckheere et al.*, 2003] for the track counts. The apatites were polished parallel to their prism faces, and between 11 and 60 crystals from each sample were counted by two analysts (J. K. and K. S.; Table S4) at 800 times magnification. In the case of the availability of two or more sample ages within one outcrop, we calculated an outcrop WMA. We measured track-length distributions for several samples. These are reported and discussed in Text S1 and Figure S2 in the supporting information.

3.4. Zircon Fission Track Analysis

Zircon fission track (ZFT) ages were obtained by the ζ calibration method using the Fish-Canyon tuff age standard and the IRMM-541 standard uranium glass. We embedded the zircons in PFA Teflon® at $\sim 325^\circ\text{C}$. For easier grinding and polishing, we encased the Teflon mounts in epoxy. After removal of the Teflon mount from the epoxy, the zircon mounts were stepwise etched with a 7:5 mixture of eutectic melt of NaOH and KOH at 228°C for 13 to 49 h. The mounts were covered with 1 cm^2 of $50 \mu\text{m}$ thick, U-free muscovite external detectors, and the age standards, unknown samples, and IRMM-541 dosimeter glasses were irradiated together in the FRM-II reactor. We etched the external detectors 30 min in 40% HF at room temperature. The mounts and the corresponding external detectors were fixed side-by-side, track-side up on glass slides, and the tracks in the external detector and the zircons were counted in transmitted light at 1500 times magnification. The counted grains have a prismatic surface and moderate U concentration; we counted 17–46 grains per mount. The ages are reported as pooled ζ ages (Table S5); separate ζ values were determined for each of the two analysts.

3.5. (U-Th)/He Zircon and Apatite Analysis

Clear zircon crystals without inclusions, impurities, or cracks were selected by using a binocular microscope and their dimensions measured for the calculation of the α -ejection correction factor [*Farley et al.*, 1996]. The selected single grains were packed in Nb tubes. We analyzed 3–5 aliquots per sample. Helium was measured in the Patterson extraction line at Universität Tübingen, Germany. The zircons were heated with a 960 nm

diode for 10 min at 20 A. We reheated and reanalyzed each grain to ensure its complete degassing in the first step; the re-extracts showed < 1% of the first signal. The U and Th concentrations were determined by isotope dilution by using the Thermo Fisher iCAP inductively coupled plasma–mass spectrometry (ICP-MS) at Tübingen. We estimated the grain mass from the measured Zr concentration, assuming 49.8 wt % Zr in zircon. The analytical uncertainties of the Zr, Th, and He measurements do not exceed 2%. In contrast, the reproducibility of the sample age constitutes a larger uncertainty. We therefore report the arithmetic mean age and 2 times the standard deviation divided by the square root of the number of measured aliquots as the sample uncertainty (Table S6). Two AHe and ZHe data each were donated by W. Amidon, with the analytics described in *Amidon and Hynek* [2010].

3.6. Rb-Sr Analysis

Isotope dilution thermal ionization mass spectrometry (TIMS) work for Rb-Sr was done at TU Bergakademie Freiberg (Table S7). We weighed the samples into Savillex screw-top containers, spiked and dissolved them in a mixture of HF and HNO₃, and processed the solutions by standard cation-exchange techniques. The isotope measurements were carried out on a Finnigan MAT 262 MS. Sr measurements were done by static multicollection; the measured compositions are normalized to ⁸⁶Sr/⁸⁸Sr = 0.1194. Precision of Rb and Sr concentrations—determined on repeated analyses of the U.S. Geological Survey whole-rock standards GSP-2 and BCR-2—is estimated at ~1%; precision of ⁸⁷Sr/⁸⁶Sr isotope ratios is ≤0.02%. The value obtained for the ⁸⁷Sr/⁸⁶Sr ratio of the NBS standard SRM 987 during the period of the analytical work was 0.710288 ± 0.000038 (*n* = 23). Rb and Sr blanks were <200 pg and are insignificant for the mineral weights used.

3.7. Rutile U-Pb Analysis

Rutile was dated via laser ablation-ICP-MS at the University of California, Santa Barbara, by using a Nu Plasma HR-ES [*Kylander-Clark et al.*, 2013], using a 40 μm laser spot, a frequency of 4 Hz, and a 20 s ablation time. Data processing used Lolite version 2.3 [*Paton et al.*, 2010], which corrects for downhole fractionation and machine drift using measurements of rutile reference material (RM) R10 [*Zack et al.*, 2011] bracketed with the unknowns. Secondary RM R19 [*Zack et al.*, 2011] and R9826J [*Kylander-Clark et al.*, 2008] were used to assess in-run precision and accuracy. The long-term reproducibility of ²³⁸U/²⁰⁶Pb and ²⁰⁷U/²⁰⁶Pb ratios in rutile measured by this technique are estimated to be better than 2%, respectively. U-Pb data were evaluated by using Isoplot (Table S8) [*Ludwig*, 2008]. Because the secondary standards yielded dates within 2% of their TIMS-determined values, we include a 2% error on the dates of unknowns measured in this study. Individual analyses were not corrected for common lead. Isochrons were calculated by reference to *Stacey and Kramers* [1975] ²⁰⁷Pb/²⁰⁶Pb values.

3.8. Closure Temperatures

We approximated *T_c* [*Dodson*, 1973] for ⁴⁰Ar/³⁹Ar amphibole (ArAm), ArWm, ArBt, ArKfs, ZFT, AFT, ZHe, and AHe by using CLOSURE [*Brandon et al.*, 1998]. All investigated ArWm samples from the gneiss-dome rocks have muscovite composition [*Schmidt et al.*, 2011; *Stearns et al.*, 2013, 2015]. Biotite and orthoclase were identified in thin sections. Amphibole (Amp) analyses from the gneiss-dome magmatic rocks yielded hornblende compositions (unpublished). Given these compositions, we based the *T_c* calculations on the diffusion parameters of *Robbins* [1972] and *Hames and Bowring* [1994] for white mica (Wm), *Grove and Harrison* [1996] for Bt, *Foland* [1994] for orthoclase, and *Harrison* [1982] for hornblende. For AFT, we used the average apatite composition of *Ketcham et al.* [1999] and for ZFT the radiation-damaged zircon model of *Brandon et al.* [1998]. For AHe and ZHe, we used the parameters of *Farley* [2000] and *Reiners et al.* [2004], respectively.

For the ⁴⁰Ar/³⁹Ar, ZHe, and AHe thermochronometers, the input parameters for the *T_c* calculations are cooling rate and effective diffusion-domain size (EDDS); for AFT and ZFT, only the cooling rate is accounted for. To approximate the EDDS of a ⁴⁰Ar/³⁹Ar sample yielding a specific age, we first estimated an average radius (*r*) based on the analyzed grain-size fraction. We then calculated the radius of the sourcing volume (EDDS) yielding the specific age from the percentage of cumulate ³⁹Ar (³⁹Ar%) by (1) and (2):

$$\text{EDDS (infinite cylinder)} = \sqrt{\frac{r^2 \pi \times 39\text{Ar}\%}{\pi}} \quad (1)$$

$$\text{EDDS (sphere)} = \sqrt[3]{\frac{1.25\pi r^3 \times 39\text{Ar}\%}{1.25\pi}} \quad (2)$$

Where 100% of the ^{39}Ar release defines the sample age, the entire grain comprises a single continuous EDDS. For an orthoclase separate, with an average radius of 100 μm , and 50% of the ^{39}Ar release defining the age, the radius of the EDDS is 79 μm . This approximation simplifies the geometry of the EDDS, relating a certain age to a single cylinder or sphere within the grain, and thus results in the estimation of a maximal T_c . Our approach assumes a homogeneous K (^{39}Ar) distribution, the same degassing behavior for all grains, and unbroken crystals. Ninety-one of the 133 $^{40}\text{Ar}/^{39}\text{Ar}$ ages are based on >75% of the total ^{39}Ar release. We ensured complete degassing by melting of the grains at the end of the step-heating experiment. For the ZHe and AHe T_c estimations, we approximated the zircon crystals by reducing them to their tetragonal prism and dipyrarnidal faces, and the apatite crystals to their hexagonal prism and pinacoidal faces. We measured weight, crystal length, and height of the dipyrarnidal faces and calculated the equivalent spherical radius from these parameters.

The cooling rates derived from our multiple thermochronometers in the gneiss domes are between ~32 and 147°C/Myr and between ~0.5 and 31°C/Myr in their hanging walls (section 4 and Figure 4). For the T_c calculations, we used site-specific cooling rates outside the domes. Inside the domes, we use an averaged 60°C/Myr—given by the three best defined multiple thermochronometer-data regressions—excepting those AFT ages postdating the approximately linear cooling paths; we assume a cooling rate of ~10°C/Myr for these samples (entrance in the APAZ at ~12 Ma, at the surface at ~0°C at 0 Ma). Typical radii of EDDS are 50–200 μm for the $^{40}\text{Ar}/^{39}\text{Ar}$ data and 50–100 μm for (U-Th)/He data. For $^{40}\text{Ar}/^{39}\text{Ar}$, the observed ranges of cooling-rate and EDDS have a similar influence on the variation of the calculated T_c , which is about 30–50°C for each of the two variables, while the T_c of the fission track and (U-Th)/He dates vary <25°C. For the Rb-Sr system, we used the empirically determined T_c of ~300°C for Bt and ~500°C for muscovite [e.g., *Armstrong et al.*, 1966]. For the U-Pb system in rutile, we use a T_c of ~500°C, based on the partial retention-temperature range of 490–640°C, determined from diffusion profiles in natural rutile [*Kooijman et al.*, 2010]; this is a first-order estimate, because short-circuit diffusion pathways—e.g., ilmenite inclusions—may result in lower T_c for some grains.

4. Results: Geothermochronology of the Eastern Central Pamir

In the following, we present our results in a regional context (Figures 1b, 2a to 2f, 3, 4, 5, and 6 and Tables S1 to S8). The grouping reflects major tectonostratigraphic units and the key sections of the eastern Central Pamir, named after the valleys (and ridges) along which we sampled.

4.1. Temperature-Time Evolution of the Eastern Sarez, Muskol, and Shatput Domes: Results and Interpretation

4.1.1. Published Cenozoic Thermometry and Geochronology

Plutons and dykes crystallized from ~35 to 15 Ma (U-Pb zircon and Ttn ages) [*Malz et al.*, 2013; *Stearns et al.*, 2015]. Lu-Hf Grt ages of ~35–26 Ma date prograde metamorphism, reflecting Grt growth at 600–650°C and 0.6–0.9 GPa [*Smit et al.*, 2014]; peak pressure-temperature (P - T) estimates are 625–700°C and 0.6–0.9 GPa [*Schmidt et al.*, 2011]. U-Th-Pb Mnz ages from the Muskol and Shatput domes cover ~24–18 and ~28–20 Ma, respectively [*Stearns et al.*, 2013]. Systematic variations in the heavy rare earth element (REE) content of these Mnz imply growth under initial Grt stability and later Grt breakdown, interpreted to reflect the change from prograde or steady state peak metamorphism to retrograde conditions at ~23–21 Ma [*Stearns et al.*, 2013]. U-Pb metamorphic Ttn ages of ~18.0–16.4 Ma date retrograde reactions and (re)crystallization closely following peak- T at 675–705°C, determined by Zr-in-Ttn thermometry [*Stearns et al.*, 2015]. In the Turakuloma area (Shatput dome; Figures 2a and 2b), Grt + sillimanite (Sil) + muscovite + Bt gneiss (A96A5k) with leucocratic veins (A96A5i) in the immediate footwall of the SMSZ provided two Rb-Sr ages of coarse-grained Wm at ~37–30 Ma [*Schmalholz*, 2004], here interpreted as relicts of prograde metamorphism. Another vein in gneiss—undeformed 18.4 ± 0.8 Ma leucogranite 96A6b (U-Pb zircon) [*Malz et al.*, 2013]—cooled through ~300°C at 17.3 ± 0.3 Ma (Rb-Sr Bt) [*Schmalholz*, 2004].

4.1.2. New Geochronology

Three ArAm separates (P15s, 96S6d, and 9919G3) from amphibolite, granodiorite, and calcsilicate gneisses from the Muskol and Shatput domes record cooling through ~569–499°C at 21 ± 1 to 19.2 ± 0.2 Ma (Figures 2a, 4a to 4c, and S1). ArAm from banded gneiss from the deepest unit of the Shatput dome cooled through ~557–538°C at 15.2 ± 0.4 (separate 220913a) to 14.6 ± 0.4 (single crystal 220913b) Ma. One ArAm separate (110913 M3; Figures 2a and S1) from the Sarez dome yielded a complex age spectrum with a WMA of 22 ± 2 Ma and an atmospheric $^{40}\text{Ar}/^{36}\text{Ar}$ intercept, which may represent cooling through ~550°C. U-Pb rutile ages are 19 ± 1 Ma

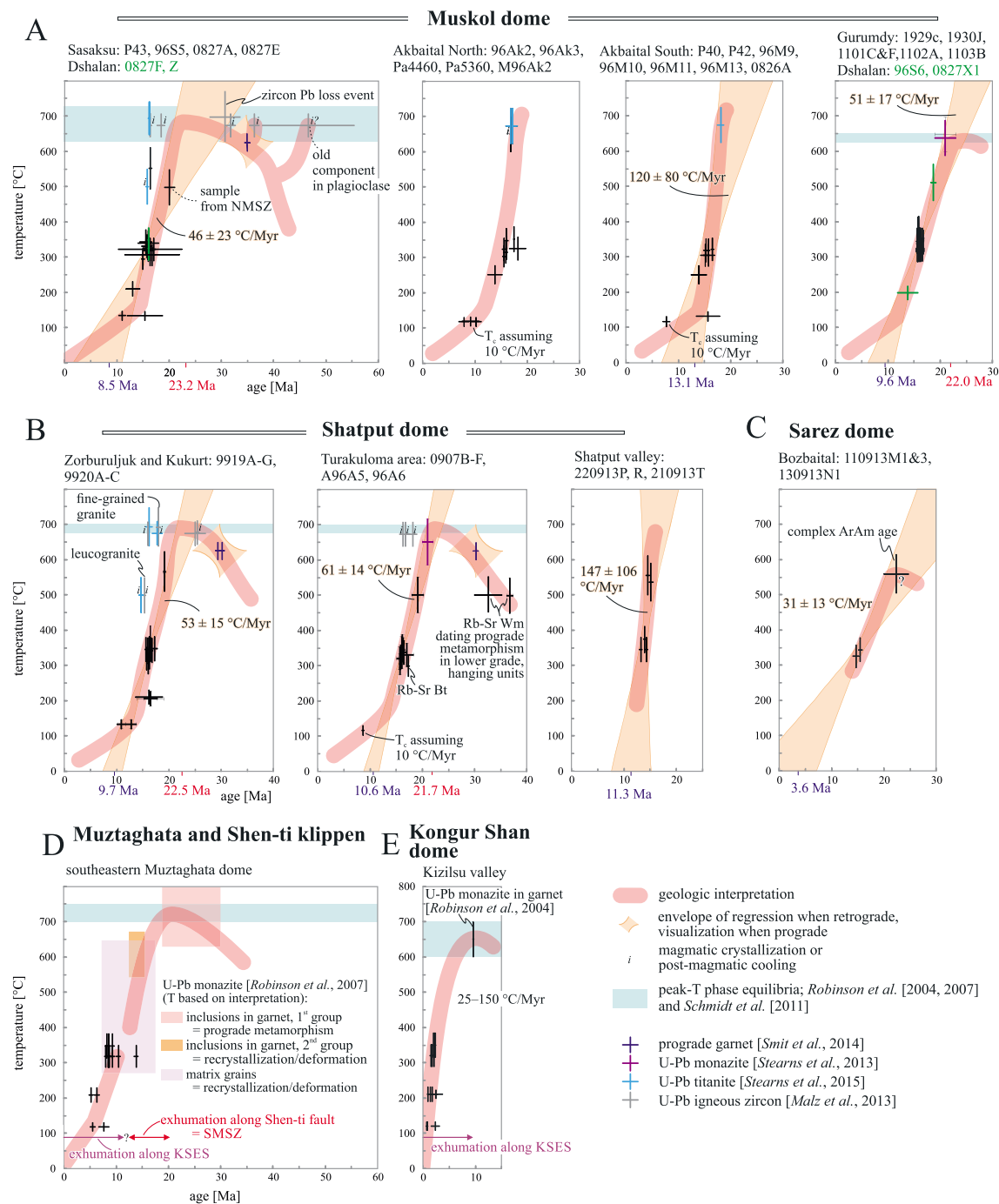
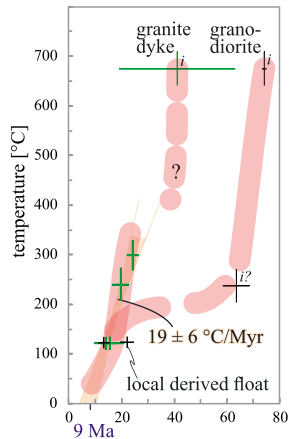


Figure 4. Temperature-time evolution of metamorphic and plutonic rocks from (a–e) the Central and East Pamir gneiss domes; (f) the Akbaital imbrications north of the gneiss domes as a part of the dome spanning Akbaital-Rangkul-Kalaktash thrust sheet; (g) the Bozbaital-Pangazdjilga fold-thrust belt south of the gneiss domes and in the footwall of the Pshart thrust system, the leading fault of the Murghab-Aksu Southeast Pamir thrust-wrench belt; and (h) the Murghab-Aksu Southeast Pamir thrust-wrench belt of the southeast Pamir. Most samples of Figure 4h are from granitoids. The areas over which data are summarized in each plot are indicated in Figure 2 by dashed frames. In Figures 4a–4c, ages interpreted to date prograde metamorphism, igneous processes, and the young (<10 Ma) AFT ages are excluded from the regressions. The blue and red ages below the abscissa indicate the intercepts of the cooling-rate regressions with surface and peak-temperature conditions, respectively. Data are compiled in Tables S2 to S8 and *Malz et al.* [2013], *Stearns et al.* [2013, 2015], and *Smit et al.* [2014]. (d) Reinterprets data of *Robinson et al.* [2007], *Sobel et al.* [2011], and *Thiede et al.* [2013]. (e) Data from *Robinson et al.* [2004, 2007], *Thiede et al.* [2013], and *Cao et al.* [2013]. Age uncertainties and envelopes of regressions are given at 2σ confidence. Uncertainty of dated temperatures are either estimated as 10% for thermochronometers or as given by independent thermometry; we assumed surface temperatures of 650–700°C for granitoids. Thermometry from *Schmidt et al.* [2011] and *Stearns et al.* [2015]. NMSZ, North Muskol shear zone; SMSZ, South Muskol shear zone; KSES, Kongur Shan extensional system; T_c , closure temperature; Bt, biotite; Wm, white mica; Am, amphibole; Kfs, K-feldspar; T-J, Triassic-Jurassic; Cr-Pg, Cretaceous-Paleogene; ZFT, zircon fission track; Ar, $^{40}\text{Ar}/^{39}\text{Ar}$; Rb, Rb-Sr.

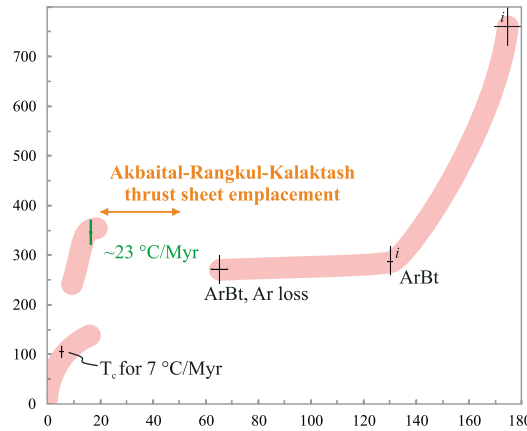
F Akbaital imbrications

Sasaksu: A96S1, 2
Akbaital North: A96K1, P17s

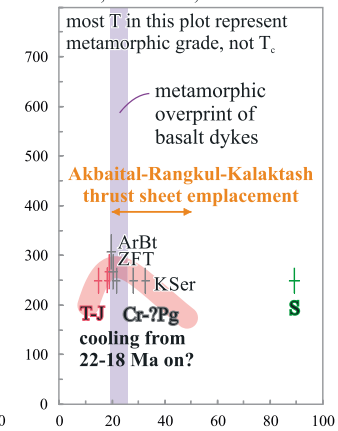


G Bozbaital-Pangazdjilga fold-thrust belt

south of Shatput dome: L96A9, L96A11



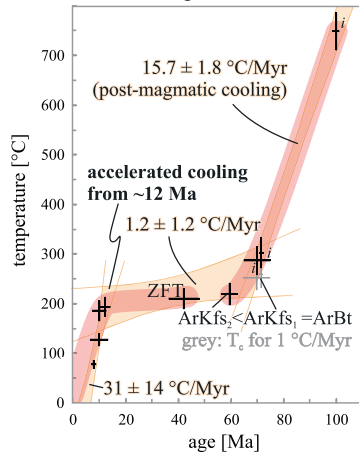
Murghab basin: L96M18, M96M5, 96M8, M96M6b, 96M7 A96M4, A96M31b, M96M28c, L96M27a, A96S2d



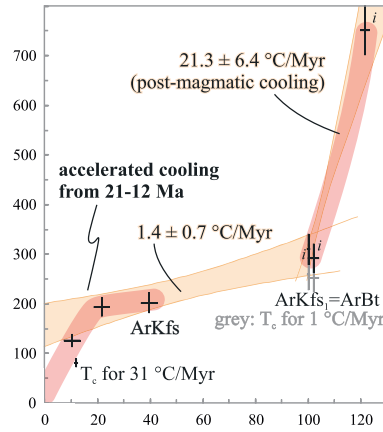
H

Murghab-Aksu-Southeast Pamir thrust-wrench belt (from W to E)

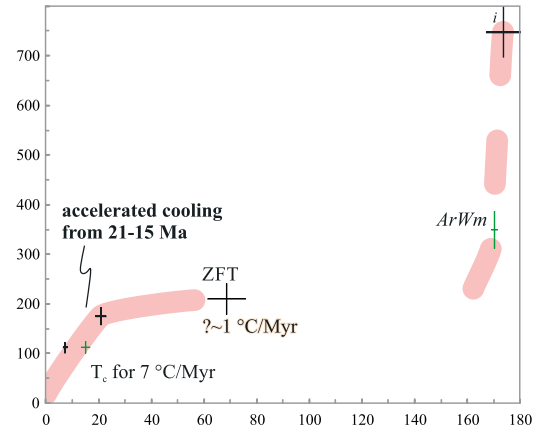
western Murghab: P5s, P912-1



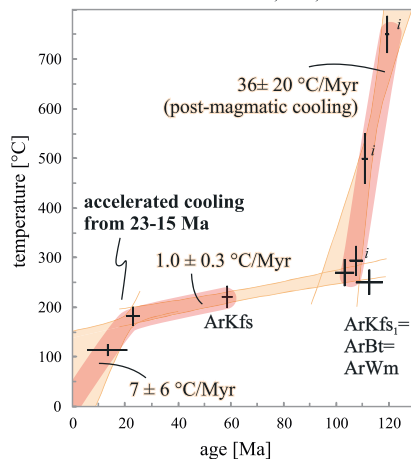
Murghab-Karasu: P2s, P912-2



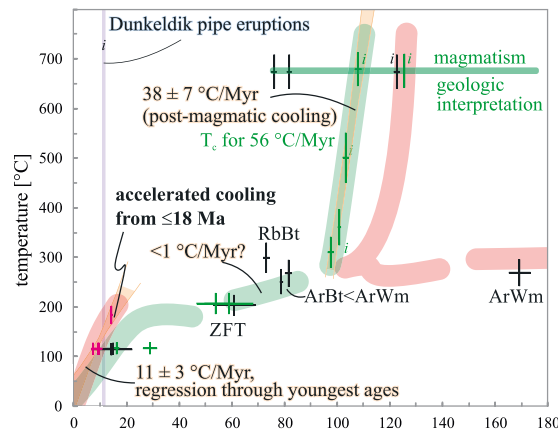
Aksu-Akbaital South: 96M25, A96M32, A96M18



western Aksu: P913-1, P7s, 4725C



Dunkeldik area: 4723C, 4724B-M, D, E, K, M, 4725A, B
eastern Aksu: M96A7, 96A10b



- geologic interpretation
- ◆ envelope of regression
- i magmatic crystallization or post-magmatic cooling

Figure 4. (continued)

(Ky-bearing micaschist 0907B1), 16.0 ± 0.3 Ma (pegmatite 0827Z3), 15.2 ± 0.3 Ma (leucogranite 9919G4), and 15 ± 1 Ma (granite 9920C1). The micaschist age records cooling after peak metamorphism; the pluton/dyke ages are within uncertainty of their U-Pb zircon crystallization ages (0827Z3 and 9919G4) [Malz *et al.*, 2013] and record postmagmatic cooling. The oldest of these highest T_c dates match the peak- T and early retrograde-condition ages of the Mnz and Ttn studies (section 4.1.1); they thus date early cooling.

Nineteen ArWm and 60 ArBt dates from micaschist, gneiss, and granite of the Sarez, Muskol, and Shatput domes show simple age spectra (Table S2 and Figures 2c and S1); their WMA and IIA are defined by $>90\%$ of the cumulative ^{39}Ar release and most have atmospheric $^{40}\text{Ar}/^{36}\text{Ar}$ intercepts. ArBt of 96M10a (paragneiss) and 96M11b (micaschist) yielded nonatmospheric $^{40}\text{Ar}/^{36}\text{Ar}$ intercepts, despite plateaus in the age spectra. These samples likely contain evenly distributed extraneous argon; we used the IIA. Ten separates define plateaus comprising $<80\%$ cumulative ^{39}Ar . In P10s, 96M9a, and 0907E1, the step ages rise with increasing heating, followed by a plateau. These samples reflect Ar loss; we report the WMA of the plateau steps. In Pa4460, Pa5360, P14sb, A96A5i, and A96A6b, the step ages decrease at the beginning of the spectrum, then define plateau steps, and—in some cases—increase at the end of the spectrum; the IIA of the plateau steps have atmospheric $^{40}\text{Ar}/^{36}\text{Ar}$ intercepts. These separates contain unevenly distributed extraneous Ar; we used the WMA for the weakly disturbed spectra and combined the uncertainties of the WMA and IIA for the more-disturbed spectra. 1104C2 and 1930F1 show plateaus interrupted by one or two outliers; vaporized organic contaminations may have interfered with the Ar measurement. We report the WMA excluding the outliers. The ArWm and ArBt ages range from 17.5 ± 0.2 to 14.0 ± 0.3 Ma and 17.0 ± 0.4 to 13.3 ± 0.3 Ma, respectively, and date cooling through $\sim 380\text{--}306^\circ\text{C}$. The ArBt ages are on average 0.25 Myr (Standard Deviation = 0.48) younger than the ArWm ages (18 samples with both micas): in 13 samples, they are equal within uncertainty; in 4 samples, ArBt is younger than ArWm; in 96A11, ArBt is older than ArWm. No systematic age differences occur between samples with the relative older $\sim\text{E-W}$ and the younger $\sim\text{N-S}$ stretching lineations in the dome rocks (Figure 2d) [Rutte *et al.*, 2017]; thus, the ages record cooling.

The $^{40}\text{Ar}/^{39}\text{Ar}$ ages of six orthoclase separates (ArKfs) from granites and orthogneisses span 16.1 ± 0.1 to 15 ± 1 Ma (Table S2 and Figures 2e and S1). In 140913P1, Pa5360, and 0907C1, all steps define the WMA and the IIA; the latter have atmospheric $^{40}\text{Ar}/^{36}\text{Ar}$ intercepts. 0827Z1 and P15s show age-step variations of a few Ma; these steps define IIA with nonatmospheric $^{40}\text{Ar}/^{36}\text{Ar}$ intercepts, likely reflecting evenly distributed extraneous Ar. The 9920A1 age spectrum shows two flat sections. We interpret the low- T one—yielding 16.6 ± 0.4 Ma—to record cooling through $\sim 305^\circ\text{C}$, and the 20 ± 2 Ma component as postmagmatic cooling of this 25.5 \pm 0.5 Ma pegmatite (U-Pb zircon) [Malz *et al.*, 2013]. T_c of ArKfs are $\sim 332\text{--}295^\circ\text{C}$. Plagioclase (Pl) from the NMSZ (gneiss 0827A1) yielded a spectrum with two flat age sections. The 17 ± 5 Ma section is similar to nearby ArWm ages and may record cooling through $\sim 300^\circ\text{C}$; the 46 ± 9 Ma component may be close to the orthogneiss crystallization age.

The 16 ± 1 to 14 ± 1 Ma ZFT ages of orthogneisses Pa4460, P8s, and P15s are identical within uncertainty to the ArBt ages and record cooling through $\sim 250^\circ\text{C}$ (Table S5 and Figure 2e). The ZHe ages of gneisses P15s and 0827X1, granite 140913P1, quartzite 9919A3, and schist 9919E range from 17 ± 3 to 13 ± 2 Ma (Table S6 and Figure 2f); their estimated T_c is $\sim 200^\circ\text{C}$. Ten AFT ages cover 16 ± 2 to 7.7 ± 0.6 Ma (Table S4 and Figure 2f). The 13 ± 1 Ma leucogranite-dyke (9920B1) age might record postmagmatic cooling (15.9 ± 0.3 Ma, U-Pb zircon) [Malz *et al.*, 2013]; all other AFT ages significantly postdate the peak metamorphism or crystallization ages and record cooling through $132\text{--}118^\circ\text{C}$.

Figures 4a–4c show regressions through the retrograde thermochronometric data and interpretations of the full T - t paths including data on magmatism and prograde metamorphism. The cooling rates from peak- T —excluding magmatic cooling—are $31\text{--}147^\circ\text{C}/\text{Myr}$. Those best defined by multiple thermochronometers over a large temperature range are 46 ± 23 , 51 ± 17 , 53 ± 15 , and $61 \pm 14^\circ\text{C}/\text{Myr}$ (Sasaku, Dshalan, and Gurumdy valleys; Figure 4a; Zorburuljuk and Kukurt valleys; and Turakuloma area; Figure 4b). In the domes, prograde metamorphism and magmatism are to first-order contemporaneous, starting at ~ 35 Ma. At $\sim 25\text{--}20$ Ma, peak- T of $\leq 700^\circ\text{C}$ were reached. The U-Pb rutile and ArAm cooling ages are systematically and slightly younger than 20 Ma. The other thermochronometric ages follow according to their T_c . Except for the eastward-younging $^{40}\text{Ar}/^{39}\text{Ar}$ ages in the Shatput dome (section 4.1.3) and the AFT ages, the age scatter of the individual thermochronometers is within uncertainty or <2 Myr. AFT is the only thermochronometer in the eastern Central Pamir gneiss domes with larger age scatter (~ 8 Myr). This implies slower and spatially nonuniform cooling through the upper $\sim 3\text{--}5$ km of the crust, contrasting to cooling through the partial annealing/retention zones of the higher- T thermochronometers.

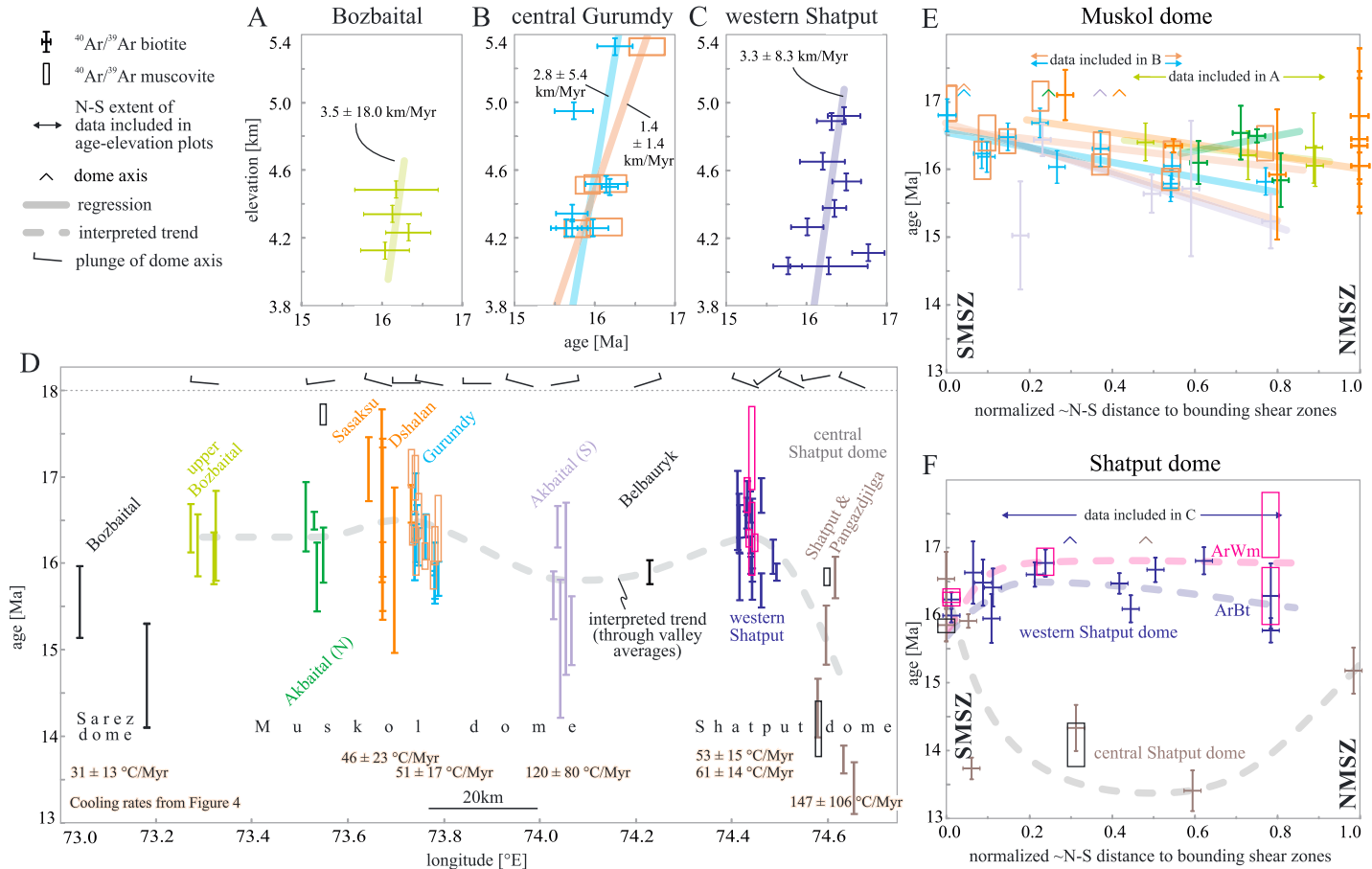
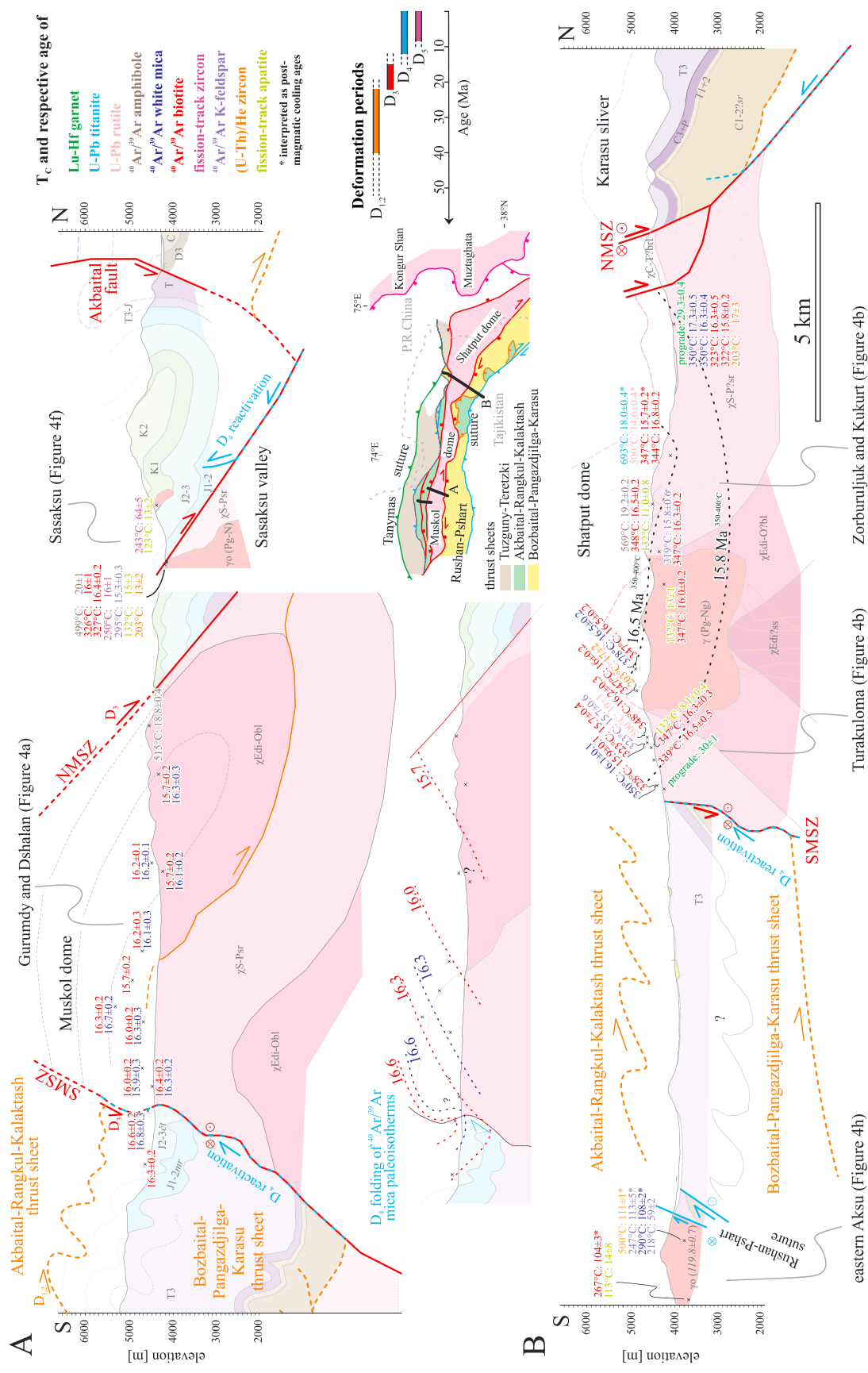


Figure 5. Three-dimensional variation of $^{40}\text{Ar}/^{39}\text{Ar}$ mica ages in the Muskol and Shatput domes. (a–c) Although ages are mostly indistinguishable within uncertainty, age-versus-elevation plots yield consistent exhumation rates at ~ 3 km/Myr. (d) Variation of ages and cooling rates (from Figure 4) along the strike of the domes. (top) Along-strike variation of the plunge of the dome crestline from *Rutte et al.* [2017]. (e and f) Variation of ages normal to the strike of the domes. The horizontal distance of each sample to the northern (the North Muskol shear zone, NMSZ) and southern dome boundaries (the South Muskol shear zone, SMSZ) is normalized, allowing comparison despite dome-width variations. Arrows indicate horizontal N-S extent of data included in Figures 5b and 5c. In Figures 5d–5f, the ages were normalized to an elevation of 4 km, using an exhumation rate of 3 km/Myr (see Figures 5a–5c).

4.1.3. Horizontal and Vertical Age Trends in the Sarez, Muskol, and Shatput Domes

Figure 5 illustrates the ArWm and ArBt age variations of the Muskol and Shatput dome samples with elevation, normal to strike, and along strike. In three areas, the mica dates cover elevations between 4117 m and 5360 m over areas small enough to minimize the influence of the horizontal trends (discussed below). Most ages are indistinguishable within 2σ uncertainty, but age-elevation regressions (Figures 5a–5c) are consistent, with slopes of 1.4–3.5 km/Myr (mostly at ~ 3 km/Myr). Too few data prohibit the definition of vertical trends from the other thermochronometers. For the ArWm and ArBt data, we used the 3 km/Myr age-elevation trend to normalize all ages to an elevation of 4 km for the discussion of the horizontal age variations (Figures 5d–5f, see also end of section); this compensates for the generally southward increasing sample elevations. The Muskol dome shows a weak eastward younging along-strike age trend (Figure 5d); the average ages are all about equal in the Bozbaital (~ 16.3 Ma), Akbaital North (~ 16.3 Ma), and Sasaksu and Gurumdy (~ 16.5 Ma) valleys and decrease to ~ 15.8 Ma in the Akbaital South valley. In the Shatput dome, the ages are ~ 16.3 Ma in the west and decrease eastward over ~ 20 km into the central Shatput dome to ~ 14.7 Ma. This eastward younging is also evident from the ArAm ages (~ 4 Myr decrease; Figure 2b). In the Muskol and western Shatput domes, the ArWm and ArBt age variation is opposite to the undulation in the dome crestline: the culminations and structurally deeper units contain the older ages, and the depressions and structurally higher units contain the younger ages. In contrast, the eastward younging ages in the central Shatput dome correlate with the west plunging dome axis, such that the youngest ages are in the structurally deepest units. The two ArBt ages from the eastern Sarez dome are ~ 1 Myr younger than the ages from the western Muskol dome.



To analyze the strike-normal age variation in the domes, we normalized the sample positions by their distance to the northern and southern dome boundaries, the NMSZ and SMSZ, respectively. Figure 5e shows the trends for each valley in the Muskol dome. The ages young northward with a dome-spanning difference of 0.5–1.5 Myr. No trend was derived for the few data south of the dome axis. Figure 5f illustrates the strike-normal age variation in the Shatput dome. In the western dome (Zorburuljuk and Kukurt valleys and Turakuloma area), the ages decrease by ~0.5 Myr northward and southward from the dome axis. In the central dome, the youngest ages occur in its center, whereas the ages close to the NMSZ and SMSZ are similar to those farther west. Figure 6 shows ~N-S cross sections through the Gurumdy valley of the Muskol dome and the western Shatput dome. Both of the described trends—downward and outward younging ages—are traced by the $^{40}\text{Ar}/^{39}\text{Ar}$ mica paleoisotherms. Their spacing is defined best in the area of the dome axis, where it suggests exhumation rates of 3–5 km/Myr. The ~30° tilting of the paleoisotherms away from the NMSZ shows its dominant control on cooling. Likely, the paleoisotherms were dipping at a much shallower angle at the time of mica closure to Ar diffusion; this justifies the above-described normalization of $^{40}\text{Ar}/^{39}\text{Ar}$ ages to elevation when trying to identify lateral trends.

4.1.4. Timing of Deformation Zones

We dated specific samples to pin down the timing of deformation. The structural data for these deformation-zone dating samples are—together with abbreviated age information—given in Figures 5 and S2 of *Rutte et al.* [2017]; therein, we also provided microstructurally derived temperature information. Several samples define parts of the slip history of the NMSZ (Table S2 and Figure S1). Fibrous Amp of westernmost Muskol-dome separate 140913M1 (Figure 2a) grew along a normal fault in calcilicite; 96% of the ^{39}Ar release, encompassing 12 steps, defines a WMA and an IIA with an atmospheric $^{40}\text{Ar}/^{36}\text{Ar}$ intercept at 17.3 ± 0.7 Ma. Biotite of 96Ak2f of the north-central Muskol dome (Figure 2a) coats—together with Chl and quartz (Qtz)—a normal fault; it released 94% of ^{39}Ar in three steps, defining a WMA and an IIA with an atmospheric $^{40}\text{Ar}/^{36}\text{Ar}$ intercept at 18 ± 2 Ma. Fibrous Amp of samples P8s and P9s from the east-central Muskol dome (Figure 2a) grew in shear zones. Single and multiple crystal separates of P8s provided disturbed age spectra with a young component at 22 ± 3 Ma from 12 low- T steps providing 22% of ^{39}Ar released, and an older component of ~80 Ma from higher- T steps. Eight steps of P9s comprise 84% of the ^{39}Ar release; they contain homogeneously distributed extraneous Ar with an IIA of 22 ± 2 Ma. Metagabbro boudins within calcilicite of the Muskol dome core (96Ak3; Figure 2a) formed within NMSZ mylonites; they were overprinted by static Bt growth and later by discrete shear zones and faults. Seventy-four percent of the ^{39}Ar release from coarse Amp crystals in the boudin defines a WMA and an IIA with an atmospheric $^{40}\text{Ar}/^{36}\text{Ar}$ intercept at 19.1 ± 0.1 Ma. The low- T steps comprise 4% of the ^{39}Ar release with an atmospheric $^{40}\text{Ar}/^{36}\text{Ar}$ intercept, and define an age of 15 ± 1 Ma; this matches the ArBt age from the same boudin and is interpreted to date the static overprint. Separates 96S6 characterize NMSZ mylonites along the northern rim of the central Muskol dome (Figure 2a) where Amp-rich boudins occur in felsic layers with ductile Pl and Qtz (Figures 6j and 6l in *Rutte et al.* [2017]). The Amp is fibrous in the boudin necks and tension gashes and occurs together with Bt and Chl; dominant prism $\langle a \rangle$ glide inferred from lattice-preferred orientation implies local high- T or—more likely—fluid-assisted Qtz ductility; thin-section microstructures indicate subgrain-rotation recrystallization in Qtz. The fibrous Amp (96S6c) is 21 ± 1 Ma and likely dates boudinage at $\geq 550^\circ\text{C}$; it is slightly older than the finer-grained Amp within the boudin (18.8 ± 0.4 Ma, 96S6d), which likely dates cooling through $\sim 515^\circ\text{C}$. Separate P10s from the northern tip of the NMSZ in the eastern Muskol dome (Figure 2a) is from brittle-ductile shear bands with fibrous Bt that localized deformation within an earlier, higher- T amphibolite mylonite; 68% of the ^{39}Ar release defines an ArBt WMA at 15.3 ± 0.4 Ma. These dates highlight synkinematic mineral growth at or below their T_c along the NMSZ, implying slip between at least 22.0 and 15.3 Ma and overlapping with the cooling ages (section 4.1.2). Two stations define late-stage slip along the SMSZ. At stations 96M10 and 96M11 (Figure 2a), mylonite of volcanoclastic gneiss and Grt-Bt schist shows brittle-ductile shear bands and tension gashes along the southern boundary of the eastern Muskol dome. ArBt of both separates (96M10a and 96M11b) from the shear bands shows spectra containing homogeneously distributed extraneous Ar with IIA at 15.1 ± 0.8 and 16 ± 1 Ma, respectively.

4.2. Thermochronology of the Hanging Wall Rocks of the North Muskol Shear Zone: Results and Interpretation

Our data are from the Akbaital imbrications, an internally faulted and folded klippe of the gneiss-dome spanning Akbaital-Rangkul-Kalaktash thrust sheet north of the Muskol dome (Figures 2, 4h, and 6a and Tables S2 to S7). The Cambrian-Paleogene strata of the klippe contain structures associated with its

Paleogene emplacement, Miocene overprint by normal faults in the hanging wall of the NMSZ, and post-NMSZ folds and thrusts, imposing top-to-~S shortening [Rutte *et al.*, 2017].

In the Sasaku valley of the central Muskol dome, diaphthoritic granodiorite A96S1b (Figure 2a) crystallized at ~74 Ma (U-Pb zircon) [Schwab *et al.*, 2004]; the ZFT and AFT ages are 64 ± 5 [Schmalholz, 2004] and 13 ± 2 Ma, respectively, likely marking postintrusion cooling and Cenozoic exhumation/cooling. Diaphthoritic granite pebble A96S1a (Figure 2a)—local float—has an AFT age of 21 ± 2 Ma; this rock—collected in a narrow gully—likely originated from the locally conglomeratic Cretaceous strata above the A96S1b granodiorite. Track lengths are one of the longest and the age is the oldest in our study. The high tectonic position of this sample in the thrust stack with little Cenozoic heating makes it likely that this age dates early cooling following prograde metamorphic apatite reset. Phonotephritic dyke A96S2d close to the NMSZ (Figure 2a) has lath-shaped Pl, serpentine pseudomorphs after olivine, and abundant opaque phases. Its 18.4 ± 0.4 Ma $^{40}\text{Ar}/^{39}\text{Ar}$ WMA comprises 16 steps with 92% of cumulative ^{39}Ar released, and a $^{40}\text{Ar}/^{36}\text{Ar}$ intercept close to atmospheric; the 18 ± 2 Ma K-Ar whole-rock age is identical. These ages likely date prograde metamorphic reset or early cooling along the NMSZ.

In the Akbaital North valley, north of the west-central Muskol dome, Jurassic quartzose schist A96K1 of the NMSZ hanging wall (Figure 2a) shows unreset or partly reset detrital ZFT ages with clusters at ~165, 242, and 370 Ma [Schmalholz, 2004] and a reset AFT age of 14 ± 2 Ma, ~4 Myr older than the AFT ages south of the NMSZ (section 4.1). The unreset or partly reset ZFT ages imply Cenozoic re-heating to less than 250–300°C. Deformed aplite dyke P17s (Figure 2a), intruding Cretaceous metaconglomerate and a sliver of crystalline rocks exposed in the footwall of a normal fault north of the NMSZ, has a lower intercept U-Pb zircon age of 41 ± 22 Ma [Schwab *et al.*, 2004], and ArBt, ZFT, and AFT ages of 24 ± 2 , 20 ± 3 , and 16 ± 3 Ma, respectively. The low-*T* ages define a cooling trend of ~21°C/Myr that intercepts surface conditions (~0°C) at ~10 Ma (Figure 4f). The dyke contains brittle-ductile shear bands and tension gashes filled with Qtz, Bt, and Ab. Although the ~41 Ma U-Pb zircon date is too imprecise to exclude a postmagmatic cooling interpretation of its ZFT and ArBt ages, we relate them to cooling from peak metamorphic heating (~24 to 16 Ma over ~300–120°C) along this NMSZ splay.

Figure 4f depicts the interpretation of the dates from the NMSZ hanging wall: the dykes cooled to temperatures of <300°C after intrusion. Beginning at ~24–21 Ma, the rocks cooled from >300°C below ~120°C at a rate of ~19°C/Myr. The narrow 15.7–13.0 Ma AFT age range indicates that the ~15 km long hanging wall section cooled uniformly below AFT closure. The intercept of this cooling trend with the surface conditions at ~10 Ma implies that the rate decreased at or after ~13 Ma, when normal shear along the NMSZ and its splays was replaced by thrusting and folding [Rutte *et al.*, 2017].

4.3. Geo-Thermochronology of the Hanging Wall of the South Muskol Shear Zone, the Bozbaital–Pangazdjilga Fold-Thrust Belt Rocks: Results and Interpretation

The Bozbaital-Pangazdjilga fold-thrust belt—the southern hanging wall of the Muskol-Shatput domes and footwall of the Akbaital-Rangkul-Kalaktash thrust sheet—is bounded in the south by the Pshart thrust system, the leading edge of the out-of-sequence Aksu-Murghab-Southeast Pamir thrust-wrench belt (Figure 2a). Rutte *et al.* [2017] observed ductile to ductile-brittle, normal-sense structures along the SMSZ, later refolded and partly overturned; locally, dextral-slip shear occurred. Posttectonic Bt, Ab, and scapolite (Scp) overgrew the structures within a few kilometer into the hanging wall of the SMSZ. Farther south, lower grade metamorphic conditions (mostly Chl and rarely Bt) prevailed.

In the Bozbaital (140913U1), Sasyksu (0828C1), and Gurumdy valleys (1930E1), and south of the Muskol-Shatput transition (1924F1; Figure 2a)—less than 1 km south of the Muskol dome—ArBt ages from Bt-Ab blast schists are 17.4 ± 0.2 to 15.6 ± 0.2 Ma—identical within uncertainty to ArBt cooling ages north of the SMSZ (Figure 2c). The age spectra (in particular 1930E1) gradually increase over the first heating steps (10–20% of ^{39}Ar release) with subsequent steps defining plateaus. South of the Shatput dome (96M11a and M96A8a; Figure 2a), the SMSZ is vertical, has dextral shear fabrics cutting Grt + Ky/Sil gneisses of the dome and low-grade Carboniferous schists, and spotted slate of its hanging wall. White mica from the immediate footwall rocks of the SMSZ provided Rb-Sr ages of ~37–30 Ma (prograde metamorphism; section 4.1.1), and an undeformed ~18 Ma vein/dyke cooled through ~300°C at 17.3 ± 0.3 Ma (section 4.1.2). In contrast, the ArWm age of partly mylonitic pegmatite vein L96A11a with dextral kinematics [Rutte *et al.*, 2017] in the

Carboniferous rocks is distinctly younger at 15.8 ± 0.1 Ma ($T_c \sim 355^\circ\text{C}$; Figure 2c). Jurassic granite L96A9 [Schwab *et al.*, 2004] and Triassic silty limestone A96A5h crop out farther south in the hanging wall of the SMSZ (Figure 2a). The L96A9 ArBt-age spectrum has two initial steps at 66 ± 6 Ma, followed by increasing ages, and a plateau at 129.1 ± 0.9 Ma (Figures 4g and S1). The L96A9 AFT age of 5.7 ± 0.6 Ma is the youngest documented in this study. L96A9 records long-lasting cooling to $\sim 300^\circ\text{C}$, resembling that of the Jurassic-Cretaceous granitoids of the southeast Pamir (section 4.). Here the Paleogene heating, required by loading due to the Akbaital-Rangkul-Kalaktash thrust sheet, was insufficient to reset the ArBt age. The young AFT age may reflect enhanced exhumation along an extensional segment of the East Pamir fault [Rutte *et al.*, 2017].

The posttectonic Bt ($\pm \text{Ab} \pm \text{Scp}$) growth indicates heating of the Chl and Bt grade metamorphic units of the SMSZ hanging wall by the hot gneiss-dome footwall during slip along the SMSZ. The southward increase of ArBt and ZFT dates—away from the SMSZ (Figures 2c and 2e)—suggests that the SMSZ near-field yields cooling, not formation ages; conversely, the ages farthest south (~ 20 Ma) likely date prograde mineral growth or cooling through T_c close to peak metamorphism. The indistinguishable ArBt ages across the footwall and hanging wall of the SMSZ indicate that little or no dip-slip postdated cooling to $< \sim 320^\circ\text{C}$ at ~ 17 Ma. This agrees with the absence of brittle normal-sense structures along the SMSZ [Rutte *et al.*, 2017]; dextral strike-slip shear along the SMSZ may be younger. Locally (Figure 6a), folded paleoisotherms hint at post-SMSZ shortening, as recorded structurally [Rutte *et al.*, 2017].

Within the Bozbaital-Pangazdjilga fold-thrust belt, the Murghab basin conglomerates, sand/siltstones, and marls unconformably cover Triassic-Jurassic strata (Figure 2a). The Murghab-basin strata have—above the last fossil-bearing Maastrichtian rocks— ≥ 500 m of clastic rocks that are likely Paleogene; metamorphism is Chl grade and increases toward the SMSZ to Bt grade. Basaltic to andesitic sills and dykes cut the Triassic-Jurassic and younger rocks [Dronov *et al.*, 2006; Rutte *et al.*, 2017]. We analyzed five samples from the Triassic-Jurassic rocks. Metasandstone 96M13, just above the SMSZ, yielded a K-Ar sericite age of 14 ± 1 Ma (Figures 2a and 2f). Farther to the south, the K-Ar sericite age of metasandstone M96M5 is 28 ± 2 Ma. Metasandstone A96M4 gave a K-Ar sericite age of 18 ± 1 Ma and a ZFT age of 19 ± 2 Ma (Figures 2a, 2e, and 2f) [Schmalholz, 2004]. East of the Akbaital South valley (Figure 2a), ArBt of Bt-Chl phyllite L96M18c is 19.3 ± 0.1 Ma (Figure 2c). Even farther east, sericite in Silurian phyllite 96M18a of the hanging Akbaital-Rangkul-Kalaktash thrust sheet—above the Murghab basin rocks (Figures 2a and 2f)—yielded a K-Ar age of 89 ± 2 Ma [Schwab *et al.*, 2004].

Three mafic dykes from the Murghab basin show variable degrees of alteration and complexity in their $^{40}\text{Ar}/^{39}\text{Ar}$ whole-rock age spectra. Metatrachybasalt L96M7b (Figures 2a and 2b) shows an intergranular fabric with carbonated and chloritized clinopyroxene in a matrix of saussuritized Pl laths with partly preserved primary twinning. The $^{40}\text{Ar}/^{39}\text{Ar}$ spectrum displays disturbed initial steps, but 30 higher- T steps encompassing 92% of the ^{39}Ar release constitute a WMA at 20.9 ± 0.2 Ma with an atmospheric $^{40}\text{Ar}/^{36}\text{Ar}$ isochron intercept. Metabasalt A96M31b has albitized Pl laths with secondary interstitial epidote and is cut by carbonate gashes, constituting $\sim 25\%$ of the rock volume. A six-step WMA of 20.0 ± 0.2 Ma for the first 81% of the ^{39}Ar release and a K/Ca ratio of ~ 1 is followed by increasing ages and an abrupt drop of the K/Ca ratio to ~ 0.2 ; the $^{40}\text{Ar}/^{36}\text{Ar}$ intercept of the plateau steps is atmospheric. The independently determined K-Ar whole-rock date is 22 ± 2 Ma (Figure 2b). Metabasalt M96M28c is the most-altered sample; Pl laths are albitized and surrounded by interstitial epidote and clinozoisite. Brownish-greenish material along the grain boundaries may be clay minerals. The age and K/Ca spectra are saddle-shaped; three steps comprising 59% of cumulative ^{39}Ar release define a WMA at 24 ± 7 Ma. Sericite from two Murghab basin metasandstones yielded K-Ar dates of 33 ± 2 (96M8c) and 22 ± 2 Ma (M96M6b); the latter sample has a ZFT date of 20 ± 2 Ma (Figures 2a, 2e, and 2f) [Schmalholz, 2004].

Samples of the Cretaceous-?Paleogene Murghab basin and its Triassic-Jurassic footwall, both part of the Bozbaital-Pangazdjilga fold-thrust belt, show greenschist-facies metamorphism with Chl and Bt growth in the Cenozoic [Rutte *et al.*, 2017]; biotite grade was reached only locally (L96M18c; Figures 2a and 2c). The Cretaceous K-Ar sericite dates from the hanging Akbaital-Rangkul-Kalaktash thrust sheet may reflect Cenozoic partial resetting of a Jurassic age associated with the Cimmerian orogeny [Schwab *et al.*, 2004; Angiolini *et al.*, 2014]. Because of their >20 Myr spread, we interpret the K-Ar sericite and ArBt dates in the Murghab basin and its footwall rocks as formation ages, dating prograde metamorphism as old as ~ 33 Ma, and reaching peak- T at ~ 22 – 18 Ma. These event times are coeval with metamorphism

in the crystalline rocks of the domes and record upper crustal thickening. The ~14 Ma K-Ar sericite age of the SMSZ is likely a cooling age, compatible with the temperature increase toward the domes (section 4.3). The disturbance of the age spectrum of metabasalt A96M31b in the >1050°C steps may reflect degassing of extraneous Ar from low-K/Ca phases, e.g., carbonate from the gashes or epidote; similarly, the coincidence of the saddle-shaped age and K/Ca spectra of metabasalt M96M28c suggests extraneous Ar release from low-K/Ca phases, superposed onto Pl degassing. Guided by the ArBt, ZFT, and K-Ar sericite ages, we interpret the 23–19 Ma whole-rock ages as greenschist-grade resetting of older protolith ages.

4.4. Thermochronology of the Murghab-Aksu-Southeast Pamir Thrust-Wrench Belt Rocks: Results and Interpretation

The dextral-transpressive, top-to-~N Murghab-Aksu-Southeast Pamir thrust-wrench belt contains the Early Jurassic Rushan-Pshart suture and Jurassic and Cretaceous magmatic arc rocks [Schwab *et al.*, 2004]; at its leading edge—the Pshart thrust system—it hosts the root zone of the Akbaital-Rangkul-Kalaktash thrust sheet [Rutte *et al.*, 2017]. Figure 4h summarizes the cooling of granitoids in the southeast Pamir (Figure 2a), spanning ~130 km along strike; it includes ages published in Schmalholz [2004], Schwab *et al.* [2004], Stübner *et al.* [2013b], and Malz *et al.* [2013]. The Rb-Sr Wm ages and most of the ArWm ages are within uncertainty of or postdate the intrusion ages by a few Myr (U-Pb zircon: M96A7, 109 ± 2 Ma; 4725C and P7s, 120 ± 2 Ma; 96A10, 126 ± 50 Ma; and L96A9, 170 ± 10 Ma). The age spectra of five ArWm separates are disturbed, with younger age steps for $\leq 50\%$ (4723C)—but mostly $\leq 20\%$ (P7s, M96A7, P5s, and 4724D)—of the ^{39}Ar release, before they develop into plateaus; two other spectra are undisturbed (P2s and 4725C). The first three steps of 4723C1b from the Dunkeldik area (Figures 2a and 2c) are at ~10 Ma, whereas the other disturbed samples have low-*T* steps between ~55 and 162 Ma. Five ZFT ages cover 69 ± 7 to 43 ± 6 Ma (Figure 2e), significantly younger than the ArWm ages. Contact metamorphic Wm + Grt + staurolite schist A96M18h from the Akbaital South valley (Figures 2a, 2c, and 4h) yielded an ArWm age of 170 ± 1 Ma. Green Amp from diaphthoritic amphibolite A96M32a farther west (Figures 2a and 2b) shows a disturbed spectrum with a WMA at 141 ± 9 Ma; the $^{40}\text{Ar}/^{36}\text{Ar}$ intercept is close to atmospheric. ArKfs samples P7s, P5s, and P2s (Figure 2a) feature younger and older plateau sections, separated by steps of increasing ages. The high-*T* WMAs are slightly younger than the crystallization of the granites; the low-*T* ages are at 59 ± 2 (P7s), 60 ± 3 (P5s), and 22 ± 3 Ma (P2s) (Figure 2e).

The ZHe, AFT, and AHe dates cover 40.0–5.8 Ma and are mostly <23 Ma. Along the southern margin of the Pshart and Aksu strike-slip duplexes (Figure 2a; samples p912-1 and 2, P2s, and P5s; western Murghab and Murghab-Karasu valleys) [Rutte *et al.*, 2017], the AFT and AHe ages cluster at 12.5–8.0 Ma (mostly at ~10 Ma). At the northern, the leading edge of the duplexes (Pshart thrust and Akbaital South valley), the 15 ± 1 Ma AFT age of sample A96M18g (Figures 2a and 2f) is from a low-*T*, fluid-assisted brittle-ductile mylonite [Rutte *et al.*, 2017]; south of it, the 7.5 ± 0.8 Ma AFT age of sample 96M25a (Triassic granitoid; Figures 2a and 2f) is from the likely deepest part of the duplexes and along a possible splay to the Pshart thrust. In the Dunkeldik area (Figure 2a; samples 4723 to 4725; Figure 2f), AFT dates are 15 ± 3 to 7.5 ± 0.8 Ma.

The high and intermediate-*T* thermochronometer ages from the granites outline postintrusion cooling at 16–38°C/Myr to ~300°C (Figure 4h). The three low-*T* steps at ~10 Ma of sample 4723C1a likely record a thermal or fluid overprint, associated with the ~11 Ma eruptions in the Dunkeldik magmatic field [Hacker *et al.*, 2005; Gordon *et al.*, 2012]. In the other samples (P7s, M96A7, P5s, and 4724D), the Ar loss over the low-*T* steps occurred at or until ~55 Ma; similarly, the low-*T* plateaus of Kfs point to a thermal overprint ending at 60–55 Ma. The derived T_c are in agreement with the qualitative multi-diffusion domain interpretation of Stübner *et al.* [2013b] for these samples (Table S2 and Figure S1). The ZFT ages overlap with these dates at 65–45 Ma. The computed cooling rate and grain-size dependent T_c , including those for low-*T* steps in ArKfs, draw a consistent cooling history from three independent thermochronometers (ArBt, ArKfs, and ZFT), indicating cooling through ~300°C in the Late Cretaceous to earliest Paleogene. We explain this trend as the result of cooling from the regional Cretaceous magmatism in the South Pamir [Schwab *et al.*, 2004], terminated by the initiation of the India-Asia collision. Neogene cooling reached up to 31°C/Myr from >210°C (Figure 4h). Its onset is best constrained in the western Murghab valley (P5s and P912-1; Figure 2a) with ~12 Ma; samples from other areas hint at an onset at 23–12 Ma (P2s and P912-2), 21–15 Ma (96M25, A96M32, and A96M18), 23–15 Ma (P913-1, P7s, and 4725C), ≤ 18 Ma (M96A7 and 96A10b), and <25 Ma

(Dunkeldik area; Figure 4h). The Neogene cooling trends (except for P5s and P912-1) extrapolate to surface conditions, indicating that the presently active cooling mechanism, i.e., erosion driven by activity along the Murghab-Aksu-Southeast Pamir thrust-wrench belt, may have been active from ~23 to 12 Ma and perhaps accelerated over the last ~12 Myr.

5. Discussion

As our understanding about how the thick Asian crust of the Pamir-Tibetan Plateau has been built is incomplete, part 1 of this paper series [Rutte *et al.*, 2017] presented the Cenozoic structural evolution of the eastern Central Pamir, detailing the geometry, kinematics, and amount of deformation. In the following, we discuss the different orogenic stages, their implications for the formation of the Pamir-Tibetan Plateau, the possible drivers for large-scale synconvergent extension, and the role of lateral extrusion, i.e., material transport from the Plateau into its western foreland. The timing and the deduction of the involved rates—reported herein—allow us to propose links between crustal deformation and processes in the underlying mantle. We first set the time brackets and rates for the evolutionary stages, and then use the full deformation-time data set to link the lithospheric evolution over the Cenozoic India-Asia collisional history in the Pamir.

5.1. Pre-Cenozoic History

A regional unconformity at the base of the Jurassic strata in the Central and southeast Pamir and map-scale folds and thrusts in the rocks below this unconformity demonstrate Cimmerian deformation [e.g., Dronov *et al.*, 2006; Angiolini *et al.*, 2014; Rutte *et al.*, 2017]. The geothermochronologic record of Cimmerian tectonics is weak, possibly due to our sampling focus on Cenozoic structures, but more probably due to the shallow crustal exposure in the southeast Pamir and the regional Cretaceous-Cenozoic overprint. Cimmerian tectonics is manifested in the Jurassic granitoids, their contact-metamorphic host-rock overprint along the Rushan–Pshart arc [Schwab *et al.*, 2004], and postemplacement cooling (Figures 4g and 4h). In addition, the thermochronology of these and the Cretaceous granitoids of the Murghab-Aksu-Southeast Pamir thrust-wrench belt records the regional Late Cretaceous postmagmatic cooling of the Andean-type arc that occupied the South Pamir, Karakorum, and Hindu Kush and stretched as far north as the Central Pamir (Figures 4f to 4h) [Schwab *et al.*, 2004].

5.2. Timing of Crustal Stacking in the Central Pamir

Rutte *et al.* [2017] showed that classical Alpine-type thrust-sheet and fold-nappe tectonics built the thick Asian crust of the Pamir. They recorded ~N-S shortening over the upper ~30–40 km of the Central Pamir crust and identified dome-spanning thrust systems: the Akbaital-Rangkul-Kalaktash and Bozbaital-Pangazdjilga-Karasu thrust sheets. At deeper crustal levels—within the crystalline rocks of the domes—large-scale, recumbent, north vergent fold nappes (wavelength of >10 km) developed. The exposed Central Pamir strata (Cambrian—likely Ediacaran—to Paleogene) are at least 7–10 km thick and were imbricated to a structural thickness of ~30–40 km in accordance with thermobarometry [Schmidt *et al.*, 2011; Stearns *et al.*, 2015]; this implies tripling of the Asian upper crust and its shortening to one third of its initial length.

When were the predominate thrust sheets and fold nappes emplaced? We obtained a 33–14 Ma sericite K-Ar age range from the stratigraphically highest metasediments of the Bozbaital-Pangazdjilga fold-thrust belt (Murghab basin; Figure 4g). We interpret the ages older than ~20 Ma as formation ages that date the Chl to Bt-grade prograde to peak metamorphism related to the emplacement of the Akbaital-Rangkul-Kalaktash thrust sheet atop the Bozbaital-Pangazdjilga fold-thrust belt; peak-*T* in the latter were reached at 22–18 Ma. Similarly, we interpret the ~24–21 Ma thermochronometric dates in the Akbaital imbrications, part of the Akbaital-Rangkul-Kalaktash thrust sheet north of the Muskol dome, as peak-*T*, prograde metamorphic and/or early cooling ages, related to onset of slip along the NMSZ.

The new ~33–20 Ma formation ages from the upper crustal thrust sheets correspond to the range of Cenozoic prograde metamorphic Lu-Hf Grt, U/Th-Pb Mnz, U-Pb Ttn (Figure 3), and Rb-Sr Wm ages from rocks of the South, Central, and East (Chinese) Pamir domes. The Lu-Hf Grt ages indicate that prograde amphibolite-facies metamorphism in the domes started before ~37 and ~35 Ma in the South and Central Pamir, respectively [Smit *et al.*, 2014]. The oldest U-Pb ages of Ttn associated with prograde reactions (Ttn to ilmenite) or enclosed in Grt are similar at ~34 and ~33 Ma, respectively [Stearns *et al.*, 2015]. The oldest U/Th-Pb Mnz ages in the eastern Central Pamir are ~28 Ma; the REE patterns of these Mnz indicate that they crystallized together with

Gr_t, i.e., that they date prograde metamorphism [Stearns *et al.*, 2013]. In the South Pamir, the oldest U/Th-Pb Mnz ages are ~37 Ma. Th-Pb Mnz ages in the North Pamir Karakul-Mazar belt rocks exposed in the East Pamir Muztaghata and Kongur Shan domes are mostly younger than ~18 Ma (Figure 3); one date is ~24 Ma (see section 5.4) [Robinson *et al.*, 2004, 2007]. In contrast, the Th-Pb Mnz ages from the Shen-ti klippe are as old as ~41 Ma (mostly younger than 35 Ma), and the age variation (prograde metamorphism until ~20 Ma) resembles the Central and South Pamir more than the North Pamir Muztaghata dome rocks (Figure 3). We interpreted the 37–30 Ma Rb-Sr Wm ages from the southernmost Shatput dome [Schmalholz, 2004] to date prograde metamorphism as well.

Our ages—from both the hanging wall rocks of the Central Pamir domes and the dome rocks—indicate that prograde metamorphism, i.e., crustal thickening, started before ~35 Ma in the Central Pamir, giving a minimum age for the initiation of crustal stacking. In the South Pamir, prograde metamorphism started before ~37 Ma, contemporaneously with the Central Pamir. This indicates distributed crustal thickening over the present ~150 km N-S extent of the South and Central Pamir. Applying the minimum of ~66% Cenozoic (mostly Paleogene) shortening over the ~50 km Central Pamir [Rutte *et al.*, 2017] and leaving the South Pamir width as it is today, or applying the Central Pamir shortening estimates to the entire South and Central Pamir, gives ~250–450 km for the N-S extent of contemporaneous distributed shortening. The >100 km shortening across the Central Pamir, likely constituting the leading edge of the crustal thickening in the Pamir-Tibetan Plateau in the Paleogene (section 5.6), was achieved at a rate of >7.6 km/Myr (35–22 Ma); if shortening occurred since the onset of the India-Asia collision at ~50 Ma and terminated at ~22 Ma, the rate is >3.6 km/Myr. These rates are less than half the rate of shortening across today's leading edge of the Pamir—the Main Pamir thrust system (~10–15 km/Myr) [Zubovich *et al.*, 2010; Ischuk *et al.*, 2013].

5.3. Pamir Doming: Timing of the Gravitational Collapse of the Central Pamir Mid-upper Crust

The Central Pamir gneiss domes—structurally akin to core complexes—were exhumed by normal-sense crustal-scale shear zones [Rutte *et al.*, 2017]. Among others, Replumaz *et al.* [2010]; DeCelles *et al.* [2011], and Stearns *et al.* [2013, 2015] suggested that the Indian slab broke off at ~25–20 Ma, likely along the transition between Greater India—the now subducted extended portion north of the Indian craton—and the Indian craton (Cratonic India) [e.g., Kufner *et al.*, 2016]. The long-lived and strong Paleogene shortening and the Indian slab breakoff imply enhanced gravitational potential energy stored in the Pamir Plateau, a thermally weakened crust, and an enhanced basal heat flow through asthenospheric upwelling, resulting in a high Moho temperature. Combined with a weak foreland upper crust, these factors likely drove gravitational collapse and the formation of metamorphic core complexes in the Plateau crust [à la Rey *et al.*, 2010; Rutte *et al.*, 2017]. Our thermochronologic data allow constraining the timing of the initiation and termination of extension-related rock exhumation/cooling, and estimates on their rates and spatial distribution.

Amphibole and Bt crystallized synkinematically in tectonites of the NMSZ at ~22–17 Ma (section 4.1.4); these ages set the minimum age range for extension in the Central Pamir. Multiple thermochronometers applied to samples from seven valleys of the Muskol-Shatput domes all suggest near-linear cooling from ~700 to 100°C at rates of 31–147°C/Myr, with rates of 50–60°C/Myr in the three best-studied areas (Figures 4a–4c). We relate these rates to tectonic unroofing along the SMSZ and NMSZ. The intercepts of the cooling trends with the peak temperatures span 25–16 Ma with the best constrained intercepts at 23–22 Ma. This time range corresponds to the onset of retrograde metamorphic reactions in the crystalline rocks of the Muskol-Shatput domes at 23–20 Ma as recorded in Ttn and Mnz [Stearns *et al.*, 2013, 2015]. The hanging wall of the NMSZ hosts distributed extensional structures [Rutte *et al.*, 2017]; there, cooling due to extension commenced at ~24–21 Ma at rates of ~19°C/Myr (section 4.2 and Figure 4f). The petrochronology of the gneiss-dome rocks, the dating of normal-sense deformation structures, the cooling history of the gneiss-dome rocks in the footwall of the NMSZ and SMSZ, and the cooling due to distributed extension in the NMSZ hanging wall all point to the onset of extension—i.e., the onset of ~N-S gravitational collapse—in the Central Pamir at ~23–20 Ma.

In the Muskol and western Shatput domes, the northward younging ⁴⁰Ar/³⁹Ar mica ages (Figures 5e and 5f) and the tilt of the paleoisotherms away from the NMSZ (Figure 6a) suggest progressive footwall uplift (rollover) due to motion along the NMSZ; this implies that the NMSZ controlled the doming process and was the principal unroofing shear zone, in accord with the structural observations and interpretations of Rutte *et al.* [2017]. Along strike, the valley-averaged ⁴⁰Ar/³⁹Ar ages vary by <1 Myr (16.5–15.8 Ma; Figure 5d) in the Muskol dome. The youngest ages occur in the eastern Muskol dome and its transition to the Shatput

dome. This area marks a major crestline depression of the domes (Figure 5d, top), a pinch in the pinch-and-swell geometry of the domes, and is accommodated by enhanced along-strike stretch in the dome hanging walls; *Rutte et al.* [2017] interpreted this area as an extensional neck zone with relatively stronger ~E-W extension accompanying dominant ~N-S extension. The observed age trend is compatible with the possibility that focused extension led to condensed isograds, i.e., younger ages near the pinch. In the western Shatput dome, and along its northern boundary, the ArWm and ArBt ages are within the same narrow range recorded in the Muskol dome. This indicates uniform along-strike exhumation along the NMSZ. From the western to the central Shatput dome, the ArAm, ArWm, and ArBt ages become ~3 Myr younger (Figures 2c and 5d). The young ages correlate with the steepest dips (~70°) along the NMSZ, the exposure of the deepest units of the Shatput dome (Figure 6b), and the largest outcropping Cenozoic intrusion of the Pamir, the ~11 Ma Tashkorgan alkaline complex (Figure 2c) [*Ke et al.*, 2006; *Jiang et al.*, 2012; *Rutte et al.*, 2017]. We relate this ~eastward younging trend to strong buckling at the end of doming, leading to steep dips of the NMSZ, SMSZ, and dome-internal units, combined with regional dextral wrenching [*Rutte et al.*, 2017]; this was followed by the intrusion of the Tashkorgan complex into the core of the dome (section 5.6 and Figure 6b).

We observed little or no offset of the $^{40}\text{Ar}/^{39}\text{Ar}$ mica ages across the SMSZ, indicating that normal slip largely predated ~16 Ma. Paleo-isotherms derived from $^{40}\text{Ar}/^{39}\text{Ar}$ mica closure possibly trace post ~16 Ma folding of the SMSZ (Figure 6a), which was also observed structurally [*Rutte et al.*, 2017]. Several thermochronometers yielded younger ages along the NMSZ, indicating prolonged extension (~16–13 Ma). The intercepts of the linear cooling trends with surface conditions are at ~12–4 Ma, with the best constrained at ~12–10 Ma (Figures 4a–4c). Within the domes, AFT is the only thermochronometer that yielded a significant spread in cooling ages (~16–8 Ma). Given the structural evidence of a late regional inversion from extension to shortening and strike-slip deformation across the Central Pamir (section 5.5) [*Rutte et al.*, 2017], we infer that there is a break-in-slope in the cooling history around AFT closure at ~12 Ma, at which time accelerated cooling of the rocks within the domes had ended; normal slip along the NMSZ must have ceased before. On a first order, this is consistent with the ~3 km/Myr exhumation rates derived from the age-elevation profiles and the paleoisotherm spacing (Figures 5a–5c and 6a). About 8–11 Myr (~23–20 to ≥ 12 Ma) of exhumation at a rate of ~3 km/Myr would have brought the gneiss-dome rocks from 30 to 40 km close to the surface. *Rutte et al.* [2017] estimated ~17–75 km of ~N-S extension across the Central Pamir, a minimum due to the inability to quantify rock-internal stretch; this equates to an extensional rate of 1.5–9.3 km/Myr. These exhumation and extension rates are averages, and the approximately linear cooling trends do not necessarily imply linear exhumation and extension rates.

5.4. Are the Shatput and Muztaghata Domes Related?

Distinct lithologies, detrital zircon clusters, structures, isotope geochemistry, and geothermochronologic ages constrain the possible correlation between the Central Pamir Shatput dome and the Chinese Pamir Muztaghata dome. *Robinson et al.* [2007] noted the continuation of the antiform of the Muskol-Shatput domes into the Muztaghata dome, which *Rutte et al.* [2017] substantiated by documenting south vergence in much of the Muskol and Shatput domes that is particularly pronounced in the Muztaghata dome (Figure 7). *Robinson et al.* [2012] used detrital U-Pb zircon dating and Nd-isotope geochemistry to show that Karakul-Mazar belt (North Pamir) strata core the Kongur Shan and Muztaghata domes. In contrast, the meta-sedimentary rocks of the Muztaghata and Shen-ti klippen (Figures 2a and 7) have distinct ~950, ~800, and 600–550 Ma U-Pb detrital zircon-age groups and relatively low ϵ_{Nd} values [*Yang et al.*, 2010; *Robinson et al.*, 2012]; both provenance tracers are characteristic of the Tibetan Qiangtang block, i.e., the Central Pamir. *Schwab et al.* [2004] found similarly low ϵ_{Nd} values in granitoids of the Central and southeast Pamir, and *Rutte et al.* [2017] reported comparable U-Pb detrital zircon age clusters in rocks of the Muskol and Shatput domes and their cover. In addition, the rock types and metamorphic grade of the Shen-ti and Muztaghata klippen correspond to those of the Sarylshilin and Beletuin suites of the Shatput and Muskol domes [*Robinson et al.*, 2007; *Stearns et al.*, 2013, 2015; *Rutte et al.*, 2017]. *Robinson et al.* [2007] and *Thiede et al.* [2013] correlated the SMSZ with the Shen-ti normal fault (Figure 2a), making the Shen-ti klippe a part of the Shatput dome. *Rutte et al.* [2017] showed that the NMSZ is the dominant fault exhuming the Muskol and Shatput domes. However, it does not continue from its strike in the Shatput dome directly eastward into the north of the Muztaghata dome; *Robinson et al.* [2007] considered a major shear zone unlikely there.

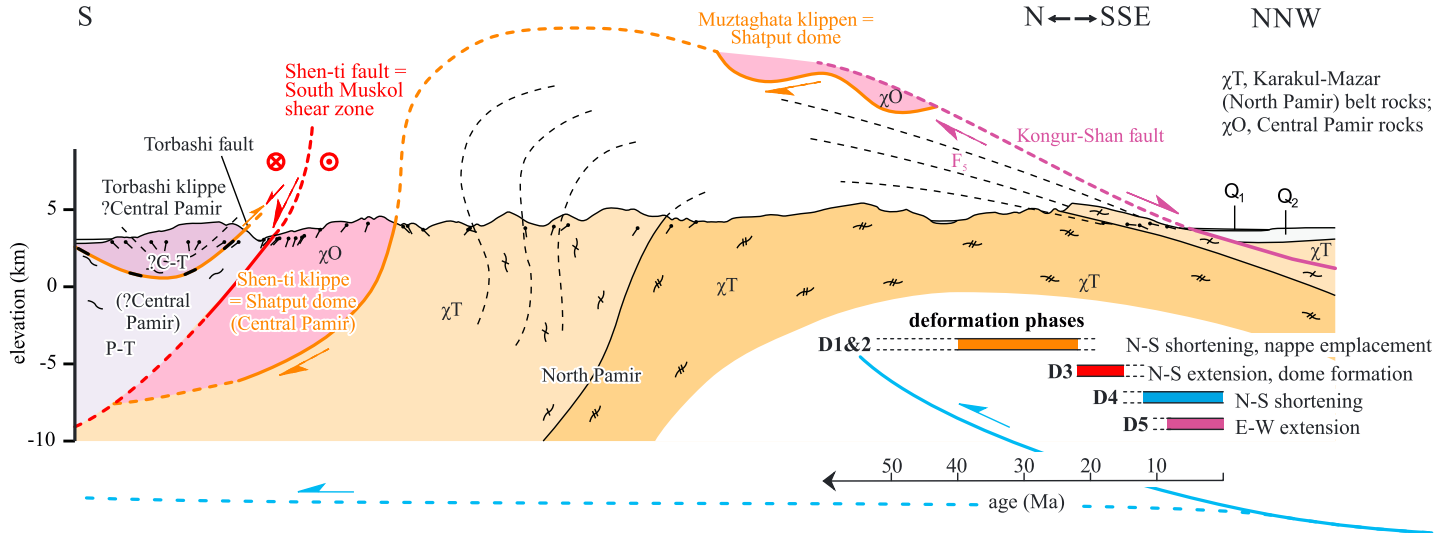


Figure 7. Cross section (trace in Figure 2a) through the Shen-ti klippe and the Muztaghata dome redrawn and reinterpreted from *Robinson et al.* [2007, 2012], and adapting the deformation phases of *Rutte et al.* [2017]. The section highlights the Paleogene underthrusting of the North Pamir Karakul-Mazar belt rocks beneath the Central Pamir (represented by the Shen-ti and Muztaghata-klippen rocks), the correlation of the Shen-ti and Muztaghata-klippen rocks with the Shatput-dome rocks, and the folding of the major structures during the fourth period of deformation (D₄). D₄ encompasses back thrusts and backfolds, which reactivate the extensional structures (D₃), that exhumed the gneiss domes. D₄ is mostly younger than ≤ 12 Ma. In this section, D₄ is interacting with ≥ 10 –0 Ma D₅ ~E-W extension along the Kongur Shan extensional system (Kongur Shan fault). Tectonic provenance, structural geometry, kinematics, and timing of the section south of the Shen-ti fault are based on the reinterpretation of the geochronologic data of *Qu et al.* [2007], *Zhang et al.* [2007], *Robinson et al.* [2007], and *Yang et al.* [2010] and are speculative. Our interpretation shows Central Pamir units south of the Muztaghata dome contrasting with the terrane correlations of *Robinson et al.* [2012]. There, amphibolite-facies rocks of the synformal Torbashi klippe thrust over greenschist-grade rocks; the stratigraphic age assignment is based on detrital and igneous U-Pb zircon ages. The Torbashi fault is either Paleogene or Cretaceous (indicated by the black stippling); it likely was reactivated by dextral-oblique normal faulting, synthetic to the Shen-ti fault (kinematic criteria in *Robinson et al.* [2007]).

Robinson et al. [2007] inferred that migmatization in the Shen-ti and Muztaghata-klippen rocks started at or close to peak-metamorphic conditions; they interpreted a group of ~ 14 (~ 16 – 11) Ma Mnz (Th-Pb Mnz Shen-ti klippe; Figure 3)—partly included in Grt—to date migmatization and prograde metamorphism until ~ 11 Ma. This interpretation would exclude the correlation of the Shen-ti and Muztaghata klippen with the Shatput dome, as such a correlation requires a common prograde metamorphism from >35 Ma on, and a switch to retrogression after ~ 23 – 20 Ma; instead, *Robinson et al.*'s [2007] interpretation extends prograde metamorphism until ~ 14 Ma. Scrutinizing the data, we suggest that the Mnz from the Shen-ti and Muztaghata klippen actually support a correlation. First, all of the Th-Pb Mnz dates included in Grt ($n = 7$) from the Muztaghata-klippen rocks are older than ~ 24.1 Ma (24.1–228.5 Ma); the matrix ages are ~ 15.9 to 7.5 Ma. In the Shen-ti klippe, all Mnz included in Grt are older than 20.6 Ma, except four grains (~ 19.2 , 14.1, 13.5, and 10.8 Ma, four additional grains with uncertainties $>40\%$ were excluded as insignificant). All matrix grains, with the exception of one (~ 119.2 Ma) are 23.6–10.3 Ma (two grains with uncertainties $>56\%$ excluded). Thus, the large majority of Mnz in Grt suggest prograde metamorphism before ~ 20 Ma; the 19.2 Ma age belongs within uncertainty to this group. We propose that the three younger Mnz were not shielded by Grt from lead loss and belong to the matrix group. The matrix Mnz may partly also date prograde or peak metamorphism (23.6–21.0 Ma), but mostly retrogression (17.8–10.3 Ma in the Shen-ti klippe and 15.9–7.5 Ma in the Muztaghata klippen). This interpretation is more consistent with the oldest ArBt cooling ages (~ 13.7 Ma; Figure 2c). Thus, the rocks of the Shen-ti klippe (Figure 3) likely record the same prograde evolution and the same ~ 20 Ma onset of exhumation/cooling by \sim N-S extension as the Muskol and Shatput domes.

We suggest that the north dipping NMSZ is offset to the north by the west dipping normal-sense Kongur Shan extensional system (Figure 2a). It may be located as indicated in Figure 2a, where younger ArWm cooling ages on the northern side of a valley (Figure 2c) could be explained by thrust reactivation of the older NMSZ, as observed in the Tajik Central Pamir [*Rutte et al.*, 2017]. The base of the Muztaghata and Shen-ti klippen represents the boundary between the Central and North Pamir, i.e., the Triassic Tanyamas suture, reactivated as the basal thrust of the Paleogene Central Pamir antiformal stack (Figure 7) [*Rutte et al.*, 2017]. In agreement with *Robinson et al.* [2012], we trace the Shatput dome—exhumed mostly during D₃ (third

deformation phase) ~N-S extension [Rutte *et al.*, 2017]—into the Muztaghata dome (Figures 2a and 7). We relate the continuous, approximately south vergent antiformal observed in both the Shatput and Muztaghata domes mostly to back thrusting/folding of D_4 [Rutte *et al.*, 2017], following D_3 ~N-S extension that exhumed the domes (Figures 2a and 7). The back thrusting/folding may temporally overlap with D_5 (~E-W extension) [Rutte *et al.*, 2017], explaining the westward protruding Muztaghata dome (Figure 2a).

Robinson *et al.* [2012] suggested—based on detrital (one sample, maximal depositional age ~253 Ma [Yang *et al.*, 2010]) and igneous (one sample, ~228 Ma meta-rhyolite [Zhang *et al.*, 2007]) zircon data, and one ϵ_{Nd} value of -9.2 [Robinson *et al.*, 2012]—that the units south of the Shen-ti fault represent metamorphosed North Pamir Karakul-Mazar rocks. Reconnaissance petrology and U-Pb zircon geochronology allow speculations on the provenance and structure south of the Shen-ti klippe (Figure 7). Qu *et al.* [2007], Wang [2008], and Yang *et al.* [2010] reported Grt-clinopyroxene-hornblende-Pl gneisses (“Grt-amphibolite and mafic granulite”) with peak and retrograde P - T conditions at 760–820°C, 1.0–1.2 GPa and 620–720°C, 0.7–0.8 GPa, respectively. The likely location of these rocks below the Shen-ti fault, and the core and rim U-Pb age groups (cores: 456 ± 30 , 480 ± 8 , 552 ± 5 Ma, and Th/U = 0.22–1.22; rims: 177 ± 6 , 181 ± 2 , 220 ± 3 Ma, and Th/U = 0.02–0.29) support Central Pamir provenance; Schwab *et al.* [2004], Robinson *et al.* [2012], and Rutte *et al.* [2017] reported similar core and (rare) rim ages in the Central Pamir. Qu *et al.* [2007] and Yang *et al.* [2010] advocated for Triassic-Jurassic peak metamorphic age, and Wang [2008] advocated for a Cambrian-Ordovician age. We speculate that the retrograde stage could be Cenozoic. Low-grade bimodal metavolcanic rocks and Ms-Qtz-Ab and Grt-Bt, partly calcareous schists south of the Shen-ti fault and north of the Torbashi fault (Kaxkorgan thrust of the Chinese literature), yielded the 228.4 ± 2.1 Ma meta-rhyolite age (see above [Zhang *et al.*, 2007]). Mafic to felsic igneous rocks occur in both the Central and South Pamir (magmatic arc rocks related to the closure of the Tanymas and Rushan-Pshart oceanic basins [Vlasov *et al.*, 1991; Schwab *et al.*, 2004]). We tentatively correlate the low-grade unit with the Central Pamir (e.g., West Pshart block), which has bimodal volcanic rocks in its Permotriassic sequence [Leven, 1995; Rutte *et al.*, 2017]. Farther south, the Torbashi fault forms the base of a high-grade, synformal klippe [Robinson *et al.*, 2007]. Detrital zircons in these Sil-Grt-Bt gneisses and graphite-bearing marbles yielded a maximum depositional age of 200–270 Ma (~200, 240–270, ~340, and 400–460 Ma age groups [Zhang *et al.*, 2007]). Yang *et al.* [2010] dated similar rocks and interpreted zircon rim ages (194 ± 1 Ma, Th/U < 0.01 and 220 ± 2 Ma, Th/U < 0.2) as dating metamorphism, youngest core ages of 253 ± 2 Ma (Th/U > 0.5) as the maximum depositional age, and 340–650 Ma zircons as older detrital grains. Such zircon-age groups occur in both the Central and South Pamir [Schwab *et al.*, 2004; Rutte *et al.*, 2017]. As large-scale, subhorizontal thrust sheets have not been documented in the Southeast Pamir yet, we speculate that the klippe of high-grade rocks is an imbricate of Central Pamir rocks, possibly rooting in the Rushan-Pshart suture, the root zone of the large Central Pamir thrust sheets, which were emplaced during the Paleogene [Rutte *et al.*, 2017]. The top-to-SW, normal-sense shear criteria along the northern Torbashi fault [Robinson *et al.*, 2007] may indicate its reactivation by faults, synthetic to the Shen-ti fault.

In the Muztaghata klippen, matrix Mnz ages are mostly ~10–8 Ma, and thus likely do not date Shatput-Muztaghata dome formation but record the northward increasing throw along the Kongur Shan extensional system [Robinson *et al.*, 2007; Thiede *et al.*, 2013]. Even farther north, at the northern tip of the Kongur Shan dome (Kizilsu; Figures 2a and 2b), six Mnz hosted in prograde Grt yielded Th-Pb ages of ~10.2–9.0 Ma; we concur with Robinson *et al.* [2004] that these date crustal thickening in the hinterland of the Main Pamir thrust system. Four matrix Mnz at ~9.0–3.6 Ma were interpreted as growth during high- T metamorphism and recrystallization during retrograde overprint [Robinson *et al.*, 2004]. Because the Main Pamir thrust system shows continuous thickening through the Recent and little exhumation, we interpret the matrix Mnz to date exhumation along the Kongur Shan extensional system; characteristically, this northern segment has the highest metamorphic grade (650–750°C, ~0.8 GPa) and the youngest Mnz along the Kongur Shan extensional system [Robinson *et al.*, 2004] and coincides with the area of the highest exhumation rates [Thiede *et al.*, 2013]. Because the suggested ~8–7 Ma onset of displacement along the Kongur Shan extensional system is based on one ArKfs multi-diffusion domain model [Robinson *et al.*, 2004], thermal modeling of ArWm and ArBt ages of ≤ 4.8 Ma [Robinson *et al.*, 2010], and lacks constraints from high- T thermochronometers, we suggest that the timing of onset of slip along the extensional system be reconsidered; it may have initiated ≥ 10 Ma and thus shortly after the cessation of the ~N-S extension in the Central and East Pamir.

5.5. Out-of-Sequence Thrusting and Dextral Wrenching

The intersection of the cooling trends of the Central Pamir gneiss-dome rocks with surface conditions between ~12 and 4 Ma (mostly 12–10 Ma) indicates that rapid cooling due to extensional exhumation until ~12 Ma was followed by a phase of slow cooling, potentially also including local re-heating. We explain this change as a result of the postextensional resumption of crustal thickening (D_4) [Rutte *et al.*, 2017], i.e., buckling of the domes, reverse-shear reactivation of the bounding shear zones, top-to-~S thrusting-folding north of the domes, and mostly top-to-~N thrusting-folding and dextral wrenching south of the domes.

Rutte *et al.* [2017] described three belts of out-of-sequence, syndoming to mostly postdoming deformation. The most prominent postdoming structure in the Central and southeast Pamir is the Murghab-Aksu-Southeast Pamir thrust-wrench belt. It is active, with dextrally oblique thrusting-folding [Strecker *et al.*, 1995; Schurr *et al.*, 2014; Rutte *et al.*, 2017]. The ZHe, AFT, and AHe ages from granitoids along its leading edge, the hanging wall of the Pshart thrust system, indicate an increase in cooling rate from near-isothermal conditions to 7–37°C/Myr starting at ~23–12 Ma; the best constrained rate change is at ~12 Ma (Figure 4h). The cooling trends extrapolate to surface conditions at ~0 Ma, suggesting that they are related to active deformation; thus, the ages represent enhanced erosion in the hanging wall of the thrust-wrench structures.

There are few direct constraints on the timing of the other two out-of-sequence, postdoming shortening belts, i.e., the Trans-Muskol transpressional back thrust zone, and the wide belt of top-to-~S thrusting-folding north of the Sarez, Muskol, and Shatput domes (from the Akbaital-Rangkul imbrications to the Karakul–Mazar belt; Figure 2a). Rutte *et al.* [2017] suggested that the concentration of the top-to-~S thrusting-folding north of the domes was caused by the exhumation of the crystalline rocks of the domes forming a rigid backstop. In any case, inversion of the extensional structures must be younger than normal slip along the NMSZ and its northerly splays. Thus, out-of-sequence thrusting-wrenching within the Central and southeast Pamir possibly interacted with extensional dome formation but was mostly younger (~16–0 Ma, mostly ≤ 12 Ma) and is still active in at least the Murghab-Aksu-Southeast Pamir thrust-wrench belt.

5.6. Tectonic Implications for the Formation of the Pamir

Figure 8 sketches the possible lithosphere-scale development of the Pamir in the framework of the western India-Asia collision zone; at ~22 Ma and 12–10 Ma significant changes in the orogen occurred. Beginning prior ~35 Ma, thrust and fold-nappe tectonics built the thick Asian crust of the Central Pamir [Rutte *et al.*, 2017] and South Pamir [Stübner *et al.*, 2013a]; petrochronologic work [Smit *et al.*, 2014; Stearns *et al.*, 2015] demonstrates their contemporaneous prograde metamorphism. Why was the Paleogene middle-upper crustal shortening distributed contemporaneously over the Central and South Pamir and likely also across the Hindu Kush and Karakorum to the south [e.g., Fraser *et al.*, 2001], while there was comparably little deformation in the North Pamir [Amidon and Hynek, 2010]? The former parts of the India-Asia collision zone constitute amalgamated Gondwana-derived terranes, whose lithosphere was rheologically weakened by a long history of subduction, arc formation, accretion, and tectonism [e.g., Guillot *et al.*, 2003; Schwab *et al.*, 2004]. Kufner *et al.* [2016] suggested that the former southern edge of the cratonic lithosphere of the Tajik and Tarim basins (Cratonic Asia) constituted the first significant obstacle for the northward progression of shortening from the India-Asia collision, because the Gondwana-terrace collage farther to the south likely lacked a rigid lithospheric keel. In the Pamir, this southern edge must have been positioned ~380 km south of its present-day position below the Central Pamir due to its northward and westward roll back since the formation of the Asian slab (Figures 1c and 8c) [Kufner *et al.*, 2016]; it likely was aligned with the southern, albeit also partly overthrust, present-day margins of the Tajik and Tarim basins west and east of the Pamir (~35–36°N). Rutte *et al.* [2017] suggested that Paleogene deformation following the collision of India with Asia quickly propagated to the southern edge of rigid Cratonic Asia and that the distinct antiformal thrust and fold-nappe stack of the Central Pamir formed south of this rheological backstop.

Following Stearns *et al.* [2013, 2015] and Rutte *et al.* [2017] ascribed the formation of the Central Pamir gneiss domes to gravitational collapse at the end of the Paleogene, which likely was triggered by the breakoff of the Greater Indian plate (Figure 8a); Stübner *et al.* [2013a, 2013b] envisioned similar processes for the South Pamir Shakh dara dome. In analogy to Rey *et al.*'s [2010] numerical experiments on gravitational collapse, the possibly >90 km thick crust, its thermally weakened state and enhanced basal heat flow (due to prolonged thickening and breakoff), and the weak foreland upper crust (due to an evaporite décollement) interacted

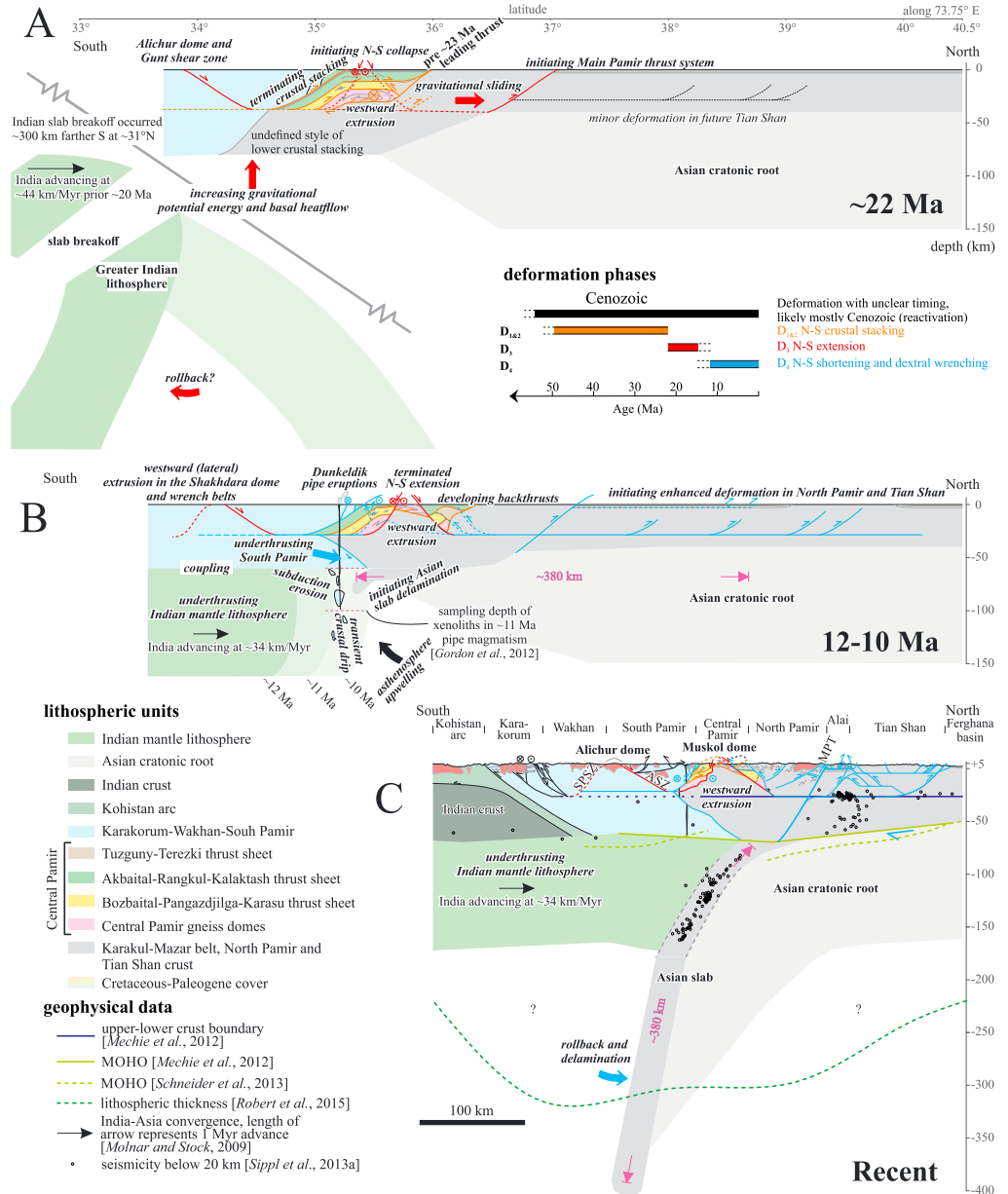


Figure 8. Three schematic sections through the western India-Asia collision zone illustrating our interpretation of the spatiotemporal relationships between crustal and mantle processes. Indian slab breakoff, underthrusting of Indian mantle lithosphere, and delamination of the Asian slab are interpreted to have driven processes acting in the crust. Active processes for each time step are in bold and italicized. The depth of the midcrustal décollement is based on the exhumation depth of the gneiss domes [Schmidt et al., 2011; Stearns et al., 2015] and a seismic discontinuity at ~27 km depth [Mechie et al., 2012]. (a) ~22 Ma: Starting prior ~37 Ma thrust sheets and fold nappes thickened the Central Pamir (and South Pamir, not shown), tripling the upper crust; North Pamir crust is underthrusting. Part of the crust is extruding laterally (westward). Greater Indian lithosphere breakoff at ~25–20 Ma triggered gravitational collapse, i.e., ~N-S extension in the South and Central Pamir. Dominant top-to-~N sliding along the North Muskol shear zone (NMSZ) initiated contraction in the North Pamir and possibly the Tian Shan. (b) ~12–10 Ma: After breakoff, Indian mantle lithosphere has been underthrusting Asia and coupling with the Pamir crust, ending ~N-S collapse and resuming N-S shortening (in the Central Pamir at ~12 Ma). Through a combination of subduction erosion and transient dripping, South Pamir rocks are buried to depth ≤ 100 km and erupted as xenoliths in the Dunkeldik volcanic pipes. At ~11 Ma Indian mantle lithosphere impinged on the southern edge of the Asian cratonic root (Tarim and Tajik basin lithosphere) and forced its delamination. (c) Recent: Delamination of the Asian slab is ongoing. Crust experiences dominant ~N-S shortening and westward extrusion through dextral wrenching and ~E-W extension (not displayed). The position of the Indian mantle lithosphere is based on Kufner et al. [2016] and retrodeformed based on the India-Asia convergence rates of Molnar and Stock [2009]. The South Pamir shear zone (SPSZ) is projected into the cross section, although it does not cross the section trace. ASZ, Alichur shear zone.

to form the metamorphic core complexes in the Pamir Plateau crust. Foreland deformation and associated sedimentation along the Main Pamir thrust system initiated at ~25–16 Ma but intensified only after ~15–10 Ma (section 2.1). We suggest that the onset of gravitational collapse of the thick, hot, and elevated Central and South Pamir crust at ~23–21 Ma explains the first pulse of foreland deformation. It triggered the relocation of the active deformation front from the Central Pamir to the North Pamir (Figure 8a). In this scenario, the significant extension along the NMSZ may imply gravitational sliding of the former (~22 Ma) edge of the Pamir Plateau onto its foreland, causing shortening (see *Rey et al.* [2010] for a numerical experiment of this scenario). In addition, this allows reinterpretation of *Amidon and Hynek's* [2010] ~25–16 Ma period of accelerated exhumation in the central North Pamir as an effect of sliding and resultant foreland shortening, enhancing erosion. Although beyond the scope of this paper, reasons for a lack of similar ~N-S extension within the Tibetan Plateau may be the absence of a weak (evaporite-floored), low-elevation foreland basin (depression), less concentrated ~N-S shortening/thickening (i.e., spread over a wider N-S distance in Tibet than in the Pamir [*Schmidt et al.*, 2011]), and the likely more southerly impact of the Indian slab breakoff; in Tibet, ~N-S extension contemporaneous with the Pamir resulted in the formation of the North Himalayan gneiss domes [*Stearns et al.*, 2013].

After breakoff of the Indian slab, the mode of convergence switched from subduction to underthrusting [*Kufner et al.*, 2016] and decreased in velocity from ~44 to ~34 km/Myr [*Molnar and Stock*, 2009]; India's northward advance then changed stresses within the overlying Asian crust from tensional back to compressional over time [*Kufner et al.*, 2016], in parallel with the decrease in gravitational potential energy resulting from collapse. Figure 8b illustrates the last stages of the envisioned course of events: Successively northward underthrusting of Cratonic India's mantle lithosphere coupled with the Pamir crust, increasing the compressive boundary forces of the orogen; ~N-S gravitational collapse then terminated in the Central Pamir at ~12 Ma, and deformation propagated into the Pamir foreland, causing intensified shortening along the North Pamir and within the Tian Shan, and out-of-sequence shortening north and south of the Central Pamir domes (section 2.1).

At ~11 Ma the Dunkeldik pipes sampled crustal xenoliths of South Pamir affinity derived from 60 to 100 km depth and comprising residues from melting at up to 1000°C (section 2.2); the xenoliths ~1000°C/2.7 GPa *T/P* ratios are lower than the ~750°C/1.0 GPa ratios characteristic of the Shakh dara-dome rocks [*Gordon et al.*, 2012], compatible with downward motion of crustal material into the mantle. *Jiang et al.* [2012] estimated a source depth for the Tashkorgan complex melts—similar to the Dunkeldik pipe melts—at ~70–100 km within the lithospheric mantle, thus at the source depth of the xenoliths. *Hacker et al.* [2005] and *Gordon et al.* [2012] suggested two mechanisms as a trigger for the deep burial of the Asian crustal xenoliths: lithospheric foundering, i.e., transient crustal drips, and/or subduction erosion. For the burial of this material, we envision a scenario that combines both mechanisms: northward bulldozing Indian cratonic mantle lithosphere induced gravitational drips at its bow. Contemporaneously, asthenospheric material was welling up—possibly induced by the underthrusting Indian mantle lithosphere—and generated the alkaline melts that enclosed the xenoliths from the crustal drips. Shortly after, at ~11 Ma, deep India impinged on deep Asia, causing the delamination and rollback of the lithosphere of the latter (Figures 8b and 8c) [*Kufner et al.*, 2016].

How does the rest of the Pamir fit into this tectonic evolution? We suggest that the early exhumation of the Shakh dara dome along the top-to-~N Gunt shear zone, beginning at ~21–20 Ma, is equivalent to exhumation in the Central Pamir domes (Figures 8a and 8b) [*Stübner et al.*, 2013b]. The ~E-W extension in the East Pamir, distributed ~E-W extension across the western Pamir Sarez-Karakul sinistral-oblique graben system, and the dextral wrenching in the Central Pamir and South Pamir since at least ~12 Ma represent an early stage of the Recent scenario, derived by *Schurr et al.* [2014] from the seismotectonics of the Pamir. They showed that dominant ~N-S shortening building the Pamir Plateau is accompanied by lateral extrusion of material into the Tajik depression west of the Plateau. The ≥90 km ~NNW-SSE extension in the Shakh dara dome and the prolonged exhumation along the South Pamir shear zone to ~4–2 Ma—well after exhumation in the Central Pamir had ceased—likely combine both: the mostly northward collapse, as envisioned for the Central Pamir and the westward collapse as indicated by the Kongur Shan extensional system and the Sarez-Karakul graben system. Characteristically, during the younger history, *Stübner et al.* [2013a] documented anticlockwise, incremental rotation of the stretching direction from ~SSE to ~SE and dextral shear zones outside the dome (e.g., the younger dextral slip history of the Gunt shear zone) concurrent during extension within the Shakh dara dome.

6. Conclusions

We establish the chronology of major Cenozoic deformation phases in the eastern Tajik Pamir to understand the timing of orogenic processes, i.e., propagation of shortening, gravitational collapse, and lateral extrusion. We explore potential underlying lithospheric and plate-scale processes that might have caused the sequence of events, i.e., slab-breakoff, underthrusting, and delamination. Amphibolite-facies metamorphism in the rocks of the Central Pamir domes and greenschist-facies metamorphism in their hanging walls are as old as ~35 Ma, indicating that early ~N-S shortening and crustal stacking had commenced by then. The short time lag of ~2–3 Myr for the earliest indications of metamorphism in the South and Central Pamir indicates rapid northward propagation of deformation, likely governed by weak rheology of the Gondwana-derived terranes between India and Cratonic Asia. Following crustal stacking, the Muskol-Shatput domes were exhumed during ~N-S extension. Synkinematic amphibole and biotite from the North Muskol shear zone—the principal unroofing structure—gave $^{40}\text{Ar}/^{39}\text{Ar}$ dates between ~22 and 17 Ma. U-Pb rutile, $^{40}\text{Ar}/^{39}\text{Ar}$ amphibole, mica, and feldspar, Rb-Sr biotite, zircon and apatite fission track, and (U-Th)/He ages document exhumation of the dome rocks from 30 to 40 km and ~700°C at average cooling rates of 50–60°C/Myr. These results agree with age-versus-elevation relationships and the spacing of paleoisotherms that indicate exhumation rates of ~3 km/Myr. The cooling trends indicate initiation of cooling at 23–21 Ma. Cooling constrained by multiple thermochronometers in the hanging wall of the extensional North Muskol shear zone similarly points to an initiation of extension at 24–21 Ma. In summary, these results indicate initiation of extension at 23–21 Ma, synchronous with the proposed slab breakoff of Greater India from Cratonic India, which likely resulted in elevated gravitational potential in the Pamir and triggered gravitational collapse. Cooling rates in the Muskol and Shatput dome decreased at ~12 Ma when the rocks cooled through closure of the apatite fission track system. At about that time, the western promontory of the India craton had thrust beneath the Pamir and coupled with the crust of the Pamir, resulting in the resumption of ~N-S shortening. These ~12 Ma to Recent thrust structures host a dextral wrenching component that—together with E-W extension—results in bulk westward extrusion of the Pamir Plateau crust into the Tajik depression. We conclude that the timing and style of deformation of the middle-upper crust of the hanging Asian plate were discontinuous and broadly controlled by dynamics of the underlying Indian and Asian lithospheres.

Acknowledgments

Data of this contribution are available in the supporting information and by contacting D.R. or L.R. DFG bundle TIPAGE (PAK 443) and BMBF bundle CAME project TIPTIMON (support code 03G0809) and US-NSF-EAR grants 0838269 and 1419751 funded this research. D.R., L.R., K.S., and S.S. received DAAD travel grants, and J.K. received a scholarship from the Faculty Development Program of AJKU, Muzaffarabad, Pakistan. Work in Tajikistan would have been impossible without the continuous support of the Tajik Academy of Sciences, in particular M. Gadoev, V. Minaev, and I. Oimahmadov. W. Amidon provided unpublished AHe and ZHe data, and E.R. Sobel liaised this donation. O. Frei helped with basalt petrography, C. Weise with Rb-Sr measurements, Y.D. Pushkarev with K-Ar analysis, and J. Hofmann with ZFT dating. M. McWilliams gave access to the Stanford Ar-laboratory in the mid-1990s, when he hosted L.R. The TIPAGE groups at GFZ Potsdam and TU Bergakademie Freiberg provided inspiring discussions. The anonymous Associate Editor, an anonymous reviewer, Stijn Glorie, and particularly A.C. Robinson improved the manuscript. We dedicate this paper to Wolfgang Frisch (Universität Tübingen), who got our work in the Pamir started in 1993 and contributed field expertise and discussions.

References

- Amidon, W. H., and S. A. Hynek (2010), Exhumational history of the north Central Pamir, *Tectonics*, 29, TC5015, doi:10.1029/2009TC002589.
- Angiolini, L., et al. (2014), From rift to drift in South Pamir (Tajikistan): Permian evolution of a Cimmerian terrane, *J. Asian Earth Sci.*, 102, 146–169, doi:10.1016/j.jseaeas.2014.08.001.
- Armstrong, R. L., E. Jäger, and P. Eberhardt (1966), A comparison of K-Ar and Rb-Sr ages on Alpine biotites, *Earth Planet. Sci. Lett.*, 1, 13–19.
- Arnaud, N. O., M. Brunel, J. M. Cantagrel, and P. Tapponnier (1993), High cooling and denudation rates at Kongur Shan, Eastern Pamir (Xinjiang, China) revealed by $^{40}\text{Ar}/^{39}\text{Ar}$ alkali feldspar thermochronology, *Tectonics*, 12, 1335–1346, doi:10.1029/93TC00767.
- Bande, A., E. R. Sobel, A. Mikolaichuk, and V. T. Acosta (2015), Talas-Fergana Fault Cenozoic timing of deformation and its relation to Pamir indentation, *Geol. Soci., London, Spec. Publ.*, 427, doi:10.1144/SP427.1.
- Bershaw, J., C. N. Garzzone, L. Schoenbohm, G. Gehrels, and L. Tao (2012), Cenozoic evolution of the Pamir plateau based on stratigraphy, zircon, provenance, and stable isotopes of foreland basin sediments at Oytay (Wuyitake) in the Tarim Basin (west China), *J. Asian Earth Sci.*, 44, 136–148, doi:10.1016/j.jseaeas.2011.04.020.
- Brandon, M. T., M. K. Roden-Tice, and J. I. Garver (1998), Late Cenozoic exhumation of the Cascadia accretionary wedge in the Olympic Mountains, northwest Washington State, *Geol. Soc. Am. Bull.*, 110, 985–1009, doi:10.1130/0016-7606(1998)110.
- Burtman, V. S., and P. Molnar (1993), Geological and geophysical evidence for deep subduction of continental crust beneath the Pamir, *Spec. Pap., Geol. Soc. Am.*, 281, 1–76.
- Cao, K., G.-C. Wang, P. V.d. Beek, M. Bernet, and K.-X. Zhang (2013), Cenozoic thermo-tectonic evolution of the northeastern Pamir revealed by zircon and apatite fission-track thermochronology, *Tectonophysics*, 589, 17–32.
- Carlson, W. D., R. A. Donelick, and R. A. Ketcham (1999), Variability of apatite fission-track annealing kinetics: I. Experimental results, *Am. Mineral.*, 84, 1213–1223.
- Chung, S.-L., D. Liu, J. Ji, M.-F. Chu, H.-Y. Lee, D.-J. Wen, C.-H. Lo, T.-Y. Lee, Q. Qian, and Q. Zhang (2003), Adakites from continental collision zones: Melting of thickened lower crust beneath southern Tibet, *Geology*, 31, 1021–1024, doi:10.1130/G19796.1.
- Coutand, I., M. R. Strecker, J. R. Arrowsmith, G. Hillel, R. C. Thiede, A. Korjenkov, and M. Omuraliev (2002), Late Cenozoic tectonic development of the intramontane Alai Valley, (Pamir-Tien Shan region, central Asia): An example of intracontinental deformation due to the Indo-Eurasia collision, *Tectonics*, 21(6), 1053, doi:10.1029/2002TC001358.
- Cowgill, E. (2010), Cenozoic right-slip faulting along the eastern margin of the Pamir salient, northwestern China, *Geol. Soc. Am. Bull.*, 122, 145–161, doi:10.1130/B26520.1.
- Dalrymple, G. B., and M. A. Lanphere (1969), *Potassium-Argon Dating: Principle, Techniques and Applications to Geochronology*, pp. 258, Freeman, San Francisco, Calif.
- DeCelles, P. G., P. Kapp, J. Quade, and G. E. Gehrels (2011), Oligocene–Miocene Kailas basin, southwestern Tibet: Record of postcollisional upper-plate extension in the Indus-Yarlung suture zone, *Geol. Soc. Am. Bull.*, 123, 1337–1362, doi:10.1130/B30258.1.
- Dodson, M. H. (1973), Closure temperature in cooling geochronological and petrological systems, *Contrib. Mineral. Petrol.*, 40, 259–274.

Paton, C., J. D. Woodhead, J. C. Hellstrom, J. M. Hergt, A. Greig, and R. Maas (2010), Improved laser ablation U–Pb zircon geochronology through robust downhole fractionation correction, *Geochem. Geophys. Geosyst.*, *11*, Q0AA06, doi:10.1029/2009GC002618.

Pfänder, J. A., B. Sperner, L. Ratschbacher, A. Fischer, M. Meyer, M. Leistner, and H. Schaeben (2014), High-resolution $^{40}\text{Ar}/^{39}\text{Ar}$ dating using a mechanical sample transfer system combined with a high-temperature cell for step heating experiments and a multicollector ARGUS noble gas mass spectrometer, *Geochem. Geophys. Geosyst.*, *15*, 2713–2726, doi:10.1002/2014GC005289.

Qu, J.-F., L.-F. Zhang, Y.-L. Ai, Z. Lü, J.-P. Wang, H. Zhou, and S.-Y. Wang (2007), High-pressure granulite from Western Kunlun, northwestern China: Its metamorphic evolution, zircon SHRIMP U–Pb ages and tectonic implication, *Sci. China Ser. D: Earth Sci.*, *50*, 961–971.

Ratschbacher, L., W. Frisch, H.-G. Linzer, and O. Merle (1991), Lateral extrusion in the eastern Alps, Part 2: Structural analysis, *Tectonics*, *10*, 257–271, doi:10.1029/90TC02623.

Reiners, P. W., T. L. Spell, S. Nicolescu, and K. A. Zanetti (2004), Zircon (U–Th)/He thermochronometry: He diffusion and comparisons with $^{40}\text{Ar}/^{39}\text{Ar}$ dating, *Geochim. Cosmochim. Acta*, *68*, 1857–1887, doi:10.1016/j.gca.2003.10.021.

Renne, P. R., R. Mundil, G. Balco, K. Min, and K. R. Ludwig (2010), Joint determination of ^{40}K decay constants and $^{40}\text{Ar}/^{40}\text{K}$ for the Fish Canyon sanidine standard, and improved accuracy for $^{40}\text{Ar}/^{39}\text{Ar}$ geochronology, *Geochim. Cosmochim. Acta*, *74*, 5349–5367.

Renne, P. R., G. Balco, K. R. Ludwig, R. Mundil, and K. Min (2011), Response to the comment by W.H. Schwarz et al. on “Joint determination of ^{40}K decay constants and $^{40}\text{Ar}/^{40}\text{K}$ for the Fish Canyon sanidine standard, and improved accuracy for $^{40}\text{Ar}/^{39}\text{Ar}$ geochronology” by P.R. Renne et al. (2010), *Geochim. Cosmochim. Acta*, *75*, 5097–5100, doi:10.1016/j.gca.2011.06.021.

Replumaz, A., A. M. Negrodo, S. Guillot, and A. Villaseñor (2010), Multiple episodes of continental subduction during India/Asia convergence: Insight from seismic tomography and tectonic reconstruction, *Tectonophysics*, *483*(1), 125–134, doi:10.1016/j.tecto.2009.10.007.

Rey, P. F., C. Teysseier, and D. L. Whitney (2010), Limit of channel flow in orogenic plateaux, *Lithosphere*, *2*(5), 328–332, doi:10.1130/L114.1.

Robbins, G. A. (1972), Radiogenic argon diffusion in muscovite under hydrothermal conditions, M.S. thesis, Brown University.

Robert, A. M. M., M. Fernández, I. Jiménez-Munt, and J. Vergés (2015), Lithospheric structures in Central Eurasia derived from elevation, geoid anomaly and thermal analysis, *Geol. Soc., London, Spec. Publ.*, *427*, doi:10.1144/SP427.10.

Robinson, A. C. (2009a), Geologic offsets across the northern Karakorum fault: Implications for its role and terrane correlations in the western Himalayan–Tibetan orogen, *Earth Planet. Sci. Lett.*, *279*, 123–130, doi:10.1016/j.epsl.2008.12.039.

Robinson, A. C. (2009b), Evidence against Quaternary slip on the northern Karakorum Fault suggests kinematic reorganization at the western end of the Himalayan–Tibetan orogen, *Earth Planet. Sci. Lett.*, *286*, 158–170, doi:10.1016/j.epsl.2009.06.025.

Robinson, A. C., A. Yin, C. E. Manning, T. M. Harrison, S.-H. Zhang, and X.-F. Wang (2004), Tectonic evolution of the northeastern Pamir: Constraints from the northern portion of the Cenozoic Kongur Shan extensional system, *Geol. Soc. Am. Bull.*, *116*(7–8), 953–974, doi:10.1130/B25375.1.

Robinson, A. C., A. Yin, C. E. Manning, T. M. Harrison, S.-H. Zhang, and X.-F. Wang (2007), Cenozoic evolution of the eastern Pamir: Implications for strain-accommodation mechanisms at the western end of the Himalayan–Tibetan orogen, *Geol. Soc. Am. Bull.*, *119*(7–8), 882–896, doi:10.1130/B25981.1.

Robinson, A. C., A. Yin, and O. M. Lovera (2010), The role of footwall deformation and denudation in controlling cooling age patterns of detachment systems: An application to the Kongur Shan extensional system in the Eastern Pamir, China, *Tectonophysics*, *496*, 28–43.

Robinson, A. C., M. Ducea, and T. J. Lapen (2012), Detrital zircon and isotopic constraints on the crustal architecture and tectonic evolution of the northeastern Pamir, *Tectonics*, *31*, TC2016, doi:10.1029/2011TC003013.

Rutte, D., J. A. Pfänder, M. Kolečka, R. Jonckheere, and S. Unterricker (2015), Radial fast-neutron fluence gradients during rotating $^{40}\text{Ar}/^{39}\text{Ar}$ sample irradiation recorded with metallic fluence monitors and geological age standards, *Geochem. Geophys. Geosyst.*, *16*, 336–345, doi:10.1002/2014GC005611.

Rutte, D., R. Lothar, S. Schneider, K. Stübner, M. A. Stearns, M. A. Gulzar, B. R. Hacker, and Project TIPAGE members (2017), Building the Pamir–Tibet Plateau—Crustal stacking, extensional collapse, and lateral extrusion in the Central Pamir: 1. Geometry and kinematics, *Tectonics*, *36*, doi:10.1002/2016TC004293.

Schmalholz, M. (2004), The amalgamation of the Pamirs and their subsequent evolution in the far field of the India–Asia collision, PhD Thesis, Eberhard Karls Universität Tübingen, Germany, *Tübinger Geowissenschaftliche Arbeiten*, *A*, *71*, 1–103.

Schmidt, J., B. R. Hacker, L. Ratschbacher, K. Stübner, M. Stearns, A. Kylander-Clark, J. M. Cottle, A. Webb, G. Gehrels, and V. Minaev (2011), Cenozoic deep crust in the Pamir, *Earth Planet. Sci. Lett.*, *312*, 411–421, doi:10.1016/j.epsl.2011.10.034.

Schneider, F. M., et al. (2013), Seismic imaging of subduction continental lower crust beneath the Pamir, *Earth Planet. Sci. Lett.*, *375*, 101–112, doi:10.1016/j.epsl.2013.05.015.

Schurr, B., L. Ratschbacher, C. Sippel, R. Gloaguen, X. Yuan, and J. Mechie (2014), Seismotectonics of the Pamir, *Tectonics*, *33*, 1501–1518, doi:10.1002/2014TC003576.

Schwab, M., et al. (2004), Assembly of the Pamirs: Age and origin of magmatic belts from the southern Tian Shan to the southern Pamirs and their relation to Tibet, *Tectonics*, *23*, TC4002, doi:10.1029/2003TC001583.

Sippel, C., et al. (2013a), Deep burial of Asian continental crust beneath the Pamir imaged with local earthquake tomography, *Earth Planet. Sci. Lett.*, *384*, 165–177, doi:10.1016/j.epsl.2013.10.013.

Sippel, C., et al. (2013b), Geometry of the Pamir–Hindu Kush intermediate-earthquake zone from local seismic data, *J. Geophys. Res. Solid Earth*, *118*, 1438–1457, doi:10.1002/jgrb.50128.

Sippel, C., L. Ratschbacher, B. Schurr, C. Krumbiegel, H. Rui, L. Pingren, and U. Abdybachev (2014), The 2008 Nura earthquake sequence at the Pamir–Tian Shan collision zone, southern Kyrgyzstan, *Tectonics*, *33*, 2382–2399, doi:10.1002/2014TC003705.

Smit, M. A., L. Ratschbacher, E. Kooijman, and M. A. Stearns (2014), Early evolution of the Pamir deep crust from Lu–Hf and U–Pb geochronology, and garnet thermometry, *Geology*, *42*, 1047–1050, doi:10.1130/G35878.1.

Sobel, E. R., and T. A. Dumitru (1997), Thrusting and exhumation around the margins of the western Tarim Basin during the India–Asia collision, *J. Geophys. Res.*, *102*, 5043–5063, doi:10.1029/96JB03267.

Sobel, E. R., L. M. Schoenbohm, R. Thiede, D. F. Stockli, M. Sudo, and M. R. Strecker (2011), Late Miocene–Pliocene deceleration of dextral slip between Pamir and Tarim: Implications for Pamir orogenesis, *Earth Planet. Sci. Lett.*, *304*, 369–378, doi:10.1016/j.epsl.2011.02.012.

Sobel, E. R., J. Chen, L. M. Schoenbohm, R. Thiede, D. F. Stockli, M. Sudo, and M. R. Strecker (2013), Oceanic-style subduction controls late Cenozoic deformation of the Northern Pamir orogen, *Earth Planet. Sci. Lett.*, *363*, 204–218, doi:10.1016/j.epsl.2012.12.009.

Sperner, B., R. Jonckheere, and J. A. Pfänder (2014), Testing the influence of high-voltage mineral liberation on grain size, shape and yield, and on fission track and $^{40}\text{Ar}/^{39}\text{Ar}$ dating, *Chem. Geol.*, *371*, 83–95, doi:10.1016/j.chemgeo.2014.02.003.

Stacey, J. S., and J. D. Kramers (1975), Approximation of terrestrial lead isotope evolution by a 2-Stage model, *Earth Planet. Sci. Lett.*, *26*, 207–221.

Stearns, M. A., B. R. Hacker, L. Ratschbacher, D. Rutte, and A. R. C. Kylander-Clark (2015), Titanite petrochronology of the Pamir gneiss domes: Implications for mid-deep crust exhumation and titanite closure to Pb and Zr diffusion, *Tectonics*, *34*, 784–802, doi:10.1002/2014TC003774.

- Stearns, M., B. R. Hacker, L. Ratschbacher, J. Lee, J. M. Cottle, and A. Kylander-Clark (2013), Synchronous Oligocene-Miocene metamorphism of the Pamir and the north Himalaya driven by plate-scale dynamics, *Geology*, *41*, 1071–1074, doi:10.1130/G34451.1.
- Strecker, M. R., W. Frisch, M. W. Hamburger, L. Ratschbacher, S. Semiletkin, A. Zamoruyev, and N. Sturchio (1995), Quaternary deformation in the Eastern Pamirs, Tadzhikistan and Kyrgyzstan, *Tectonics*, *14*, 1061–1079, doi:10.1029/95TC00927.
- Stübner, K., et al. (2013b), The giant Shakh dara migmatitic gneiss dome, Pamir, India–Asia collision zone: 2. Timing of dome formation, *Tectonics*, *32*, 1404–1431, doi:10.1002/tect.20059.
- Stübner, K., L. Ratschbacher, D. Rutte, K. Stanek, V. Minaev, M. Wiesinger, R. Gloaguen, and Project TIPAGE members (2013a), The giant Shakh dara migmatitic gneiss dome, Pamir, India–Asia collision zone: 1. Geometry and kinematics, *Tectonics*, *32*, 948–979, doi:10.1002/tect.20057.
- Thiede, R. C., E. R. Sobel, J. Chen, L. M. Schoenbohm, D. F. Stockli, M. Sudo, and M. R. Strecker (2013), Late Cenozoic extension and crustal doming in the India-Eurasia collision zone: New thermochronologic constraints from the NE Chinese Pamir, *Tectonics*, *32*, 763–779, doi:10.1002/tect.20050.
- Thompson, J. A., D. W. Burbank, T. Li, J. Chen, and B. Bookhagen (2015), Late Miocene northward propagation of the northeast Pamir thrust system, northwest China, *Tectonics*, *34*, 510–534, doi:10.1002/2014TC003690.
- Vermeesch, P. (2012), On the visualization of detrital age distributions, *Chem. Geol.*, *312–313*, 190–194, doi:10.1016/j.chemgeo.2012.04.021.
- Vlasov, N. G., Y. A. Dyakov, and E. S. Cherev (Eds.) (1991), *Geological Map of the Tajik SSR and Adjacent Territories, 1:500,000, Vsesojuznoi Geol. Inst. Leningrad, Saint Petersburg.*
- Wang, J.-P. (2008), Geological features and tectonic significance of mélange zone in the Taxkorgan area, West Kunlun (in Chinese with English abstract), *Geol. Bull. China*, *27*, 2057–2066.
- Wei, H.-H., Q.-R. Meng, L. Ding, and Z.-Y. Li (2013), Tertiary evolution of the western Tarim basin, northwest China: A tectono-sedimentary response to northward indentation of the Pamir salient, *Tectonics*, *32*, 558–575, doi:10.1002/tect.20046.
- Yang, W.-Q., L. Liu, Y.-T. Cao, C. Wang, S.-P. He, R.-S. Li, and X.-H. Zhu (2010), Geochronological evidence of Indosinian (high-pressure) metamorphic event and its tectonic significance in Taxkorgan area of the Western Kunlun Mountains, NW China, *Sci. China Ser. D: Earth Sci.*, *53*, 1445–1459, doi:10.1007/s11430-010-4081-1.
- Zack, T., D. F. Stockli, G. L. Luvizotto, M. G. Barth, E. Belousova, M. R. Wolfe, and R. W. Hinton (2011), In situ U–Pb rutile dating by LA-ICP-MS: ²⁰⁸Pb correction and prospects for geological applications, *Contrib. Min. Pet.*, *162*, 518–530, doi:10.1007/s00410-011-0609-4.
- Zhang, C. L., S. N. Lu, H. F. Yu, and H. M. Ye (2007), Tectonic evolution of the Western Kunlun orogenic belt in northern Qinghai-Tibet Plateau: Evidence from zircon SHRIMP and LA-ICP-MS U–Pb geochronology, *Sci. China, Ser. D Earth Sci.*, *50*, 825–835.
- Zubovich, A. V., et al. (2010), GPS velocity field for the Tien Shan and surrounding regions, *Tectonics*, *29*, TC6014, doi:10.1029/2010TC002772.